TECHNISCHE UNIVERSITÄT WIEN

Diplomarbeit

Methanol Dampfreformierung mittels Perowskit Katalysatoren

Ausgeführt am Institute für Materialchemie (IMC)

der Technischen Universität Wien (TU Wien)

eingereicht von

Tobias Berger

unter Anleitung von

Univ.Prof. Mag.rer.nat. Dr.rer.nat. Christoph Rameshan

Projektass.in(FWF) Dr.in Noelia Barrabés

April 18, 2023

[redacted]

Tobias Berger

“

Ich habe nicht versagt. Ich habe nur 10.000 Wege gefunden, die nicht funktionieren.

”

– Thomas A. Edison

Acknowledgement

I would like to thank all members of the TUCAS research group for their support in carrying out my diploma thesis. In particular, I would like to thank my laboratory supervisors Projektass. Dipl.-Ing. Florian Schrenk, Projektass. Dipl.-Ing. and Hedda Drexler as well as my main supervisor Univ. Prof. Mag.rer.nat. Dr.rer.nat. Christoph Rameshan for their assistance and guidance in setting up and configuring a mass spectrometer.

In Addition, I want to thank my whole family and friends who helped and guided me through my bachelor as well as my master studies.

Statutory Declaration

I hereby declare that I have completed this diploma thesis independently and that no other aids have been used than those I have cited as sources. Literal and analogous quotations have been marked accordingly.

Vienna, 18.04.2023

Tobias Berger

Abstract

Methanol **S**team **R**eforming (MSR) provides a promising solution for the crucial fight against climate change. It holds high potential regarding the on-demand production of H_2 for the utilization as an energy carrier in e.g.: **P**roton **E**xchange **M**embrane **F**uel Cells (PEMFC). Due to high reaction temperatures required and possible formation of carbon monoxide caused by occurring side reactions the use of suitable catalysts is of crucial importance. A promising class of materials are perovskite type oxides, with a general formula of ABO_3. These materials generally display high resistance against agglomeration of nanoparticles socketed in the surface. The composition of the catalyst can be specifically modified with suitable doping materials for the A- or B-site. In this way, exsolved nanoparticles can be formed on their surfaces which fit the requirements necessary for MSR.

In this thesis different B-site doped (B = Cu, Ni, Co) perovskite type oxide catalysts with a general formular of $Nd_{0.6}Ca_{0.4}Fe_{1-x}B_xO_3$ and $Pr_{0.6}Ca_{0.4}Fe_{1-x}B_xO_3$ (Cu: x = 0.03, 0.05, 0.1 / Ni, Co: x = 0.1) as well as the undoped basic structures, were examined concerning their suitability for catalysing MSR and their behaviour during reaction conditions. The on-set temperature of the reaction combined with the selectivity towards MSR of the individual catalyst were of particular interest. Since the reaction atmosphere is saturated with water under the prevailing reaction conditions, quantification of the reaction components proved to be challenging. For this reason, a calibration strategy for a **M**ass **S**pectrometer (MS) was employed in combination with the development of a Python toolkit for an automated evaluation of the acquired data. This allowed the comparison of the catalytic activities of the investigated materials using the obtained quantitative data of possible formation of H_2 and CO. Additionally, *operando* XRD measurements were conducted at the beamline P02.1. at DESY (**D**eutsches **E**lektronen **Sy**nchrotron) to investigate possible phase changes during the reaction.

This work could demonstrate that each investigated perovskite exhibited catalytic activity regarding the on-set temperature and yield of the desired products. Doping the B-site with Cu, Ni and Co could be tied to an increase of the catalytic activity. The unwanted formation of CO could be observed at higher temperatures for all investigated materials, the degree depending on the basic structure and the dopant element used. Of the material combinations tested, the catalyst groups doped with Cu including $Nd_{0.6}Ca_{0.4}Fe_{1-x}Cu_xO_3$ and $Pr_{0.6}Ca_{0.4}Fe_{1-x}Cu_xO_3$ (x = 0.03, 0.05, 0.1), excelled to their high selectivity of 100% at temperatures of up to 350°C. This high selectivity combined with a high catalytic activity at lower temperatures make Cu based materials particularly interesting for future research in the field of Methanol Steam Reforming.

Zusammenfassung

Methanol Dampfreformierung (MSR) bietet eine vielversprechende Lösung für den entscheidenden Kampf gegen den Klimawandel, aufgrund des hohen Potenzials zur Produktion von Wasserstoff für die Nutzung als Energieträger. Aufgrund der erforderlichen hohen Reaktionstemperaturen und möglicher auftretender Nebenreaktionen, ist der Einsatz geeigneter Katalysatoren von entscheidender Bedeutung. Eine vielversprechende Materialklasse sind Perowskit-basierte Oxide mit einer allgemeinen Formel von ABO_3. Mit geeigneten Dotierungsmaterialien für die A- oder B-Stelle kann die Zusammensetzung des Katalysators gezielt modifiziert werden, um den für MSR erforderlichen Anforderungen zu entsprechen.

In dieser Arbeit wurden verschiedene B-Stellen-dotierte (B = Cu, Ni, Co) Oxidkatalysatoren mit einer allgemeinen Formel von $Nd_{0.6}Ca_{0.4}Fe_{1-x}B_xO_3$ und $Pr_{0.6}Ca_{0.4}Fe_{1-x}B_xO_3$ (Cu: x = 0.03, 0.05, 0.1 / Ni, Co: x = 0.1), sowie deren undotierte Grundstrukturen hinsichtlich ihrer Eignung zur Katalyse von MSR untersucht. Von besonderem Interesse, war hierbei die Starttemperatur der Reaktion, in Verbindung mit der Selektivität der jeweiligen Katalysatoren gegenüber MSR. Da die Reaktionsatmosphäre unter den vorherrschenden Reaktionsbedingungen mit Wasser gesättigt ist, gestaltete sich die Quantifizierung der Reaktionskomponenten herausfordernd. Aus diesem Grund wurde eine Kalibrierungsstrategie für ein Massenspektrometer (MS), in Kombination mit der Entwicklung eines Python-Toolkits zur automatisierten Auswertung der erfassten Daten, angewendet. Dies ermöglichte den Vergleich der katalytischen Aktivitäten der untersuchten Materialien, anhand der so erhaltenen quantitativen Datensätze. Zusätzlich wurden *operando* XRD-Messungen an der Beamline P02.1. am DESY (Deutsches Elektronen Synchrotron) durchgeführt, um mögliche Phasenänderungen während der Reaktion zu untersuchen.

Es konnte gezeigt werden, dass sämtliche Materialien katalytische Aktivität bezüglich Temperatur und Ausbeute der gewünschten Produkte aufwies. Die Dotierung der B-Stelle mit Cu, Ni und Co konnte mit einer Erhöhung der katalytischen Aktivität in Verbindung gebracht werden. Die unerwünschte Bildung von CO konnte bei höheren Temperaturen für alle untersuchten Materialien beobachtet werden, wobei das Ausmaß von der Grundstruktur und dem verwendeten Dotierungselement abhängig war. Von den getesteten Materialkombinationen stachen besonders die Katalysatorgruppen $Nd_{0.6}Ca_{0.4}Fe_{1-x}Cu_xO_3$ und $Pr_{0.6}Ca_{0.4}Fe_{1-x}Cu_xO_3$ (x = 0.03, 0.05, 0.1) durch ihre hohe Selektivität von 100 % bei Temperaturen von bis zu 340 °C hervor. Diese hohe Selektivität in Kombination mit einer hohen katalytischen Aktivität bei niedrigeren Temperaturen machen Cu-basierte Materialien besonders interessant für die zukünftige Forschung auf dem Gebiet der Methanol-Dampfreformierung.

Table of Contents

1. Introduction

1. Introduction

The focus of the public, world governments and also industry is increasingly directed towards renewable energy sources and a carbon-neutral future in order to limit global warming to a maximum of 1.5 °C to 2 °C. In order to actually achieve this common goal, drastic measures are required. The will to achieve this goal is demonstrated by ambitious projects such as the European Green Deal of the European Union [1], aiming for being the first climate neutral continent or the Paris Climate Protection Agreement [2] of the world community. The latest developments in the energy crisis in Europe and the rest of the world also illustrates how important it is to break away from dependence on fossil raw materials and rather build on renewable energy sources for a sustainable and secure future.

An important step towards achieving these goals is the decarbonization of energy sources, meaning the elimination of emitting CO_2 during the energy production. Apart from the industry sector and the generation of electricity and heat, a large proportion of CO_2 emissions are caused by freight and individual transport. This sector is responsible for up to 30 % of all CO_2 emissions within the EU, according to a survey conducted by the European Parliament [3]. To achieve a notable reduction in CO_2 emissions in this sector, there has been increased investment in the development and establishment of battery-powered electric vehicles (BEV) in recent years. One example would be the increasing number of companies investing in the electrification of their products, such as BMW and Volkswagen as well as the formation of new companies in the car sector solely selling an electric future, e.g. Tesla. However, this technology has serious shortages such as a short driving range and relatively long charging time compared to combustion engines. In addition to these shortcomings, another big disadvantage is the energy per unit mass. According to Thomas [4], the available energy per unit mass of batteries is significantly lower compared to hydrogen-powered fuel cells, as illustrated in Figure 1. Furthermore, utilizing this technology for freight transport poses another challenge. Transporting heavy loads over long distances takes a lot of energy. In this case, the required battery mass would increase drastically with the required energy density, which makes it difficult to utilise this technology. [4]

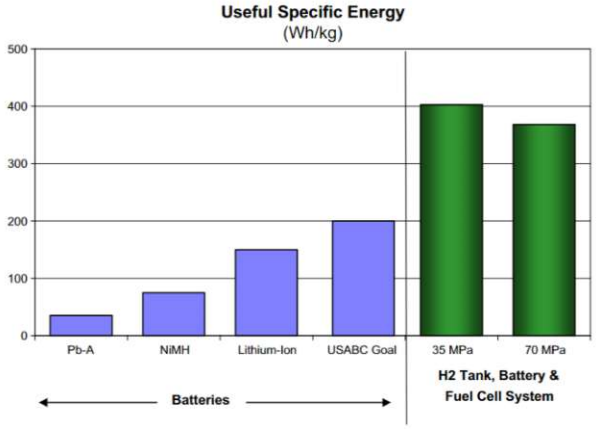

Figure 1 – Useful Specific Energy of Batteries and Fuel Cells Comparison of the energy per unit mass of different types of batteries as well as hydrogen powered fuel cells. Illustration of the higher useful specific energy of fuel cells compared to standard battery materials. Taken from Thomas [4]

For this reason, the promotion of research and development of **F**uel **C**ells (FC) has increased in the past years. FCs take advantage of being a form of electromobility, therefore reducing the CO_2 imprint of transportation, without the shortages of having short ranges and long recharging cycles. Furthermore, their higher energy density (see Figure 1) makes this technology superior to BEVs, especially for long-distance travel and heavy haulage. Unlike batteries, FCs do not store electrical energy, but rather produce it on demand utilizing low-to-zero emission fuels, such as H_2, thereby, achieving ranges comparable to combustion engine driven vehicles. The most common hydrogen-powered FC is the **P**roton **E**xchange **M**embrane **F**uel **C**ell (PEMFC) [5]. But challenges of this technology include the high energy consumption linked to the preferred production of green H_2 stemming from the production via electrolysis using electricity from renewable sources. In addition, the storage situation for H_2 over a long period of time is also complex due to occurring diffusion caused by its small atomic size. [6]

A possible solution to these problems is the on-demand production of the energy carrier H_2. In recent years promising research had been done on such on-demand systems [7] [8] [9] [10]. Opposed to storing H_2 in complex hyperbaric tanks, the energy carrier is accessed through precursor compounds, such as methanol and is released when necessary. One system with high potential is the reaction of MSR, which reacts methanol and water to H_2 and CO_2 in a favourable ratio. However, this reaction has several drawbacks. Due to its endothermic nature, high reaction temperatures are associated with methanol steam reforming. As a result of this high temperature environment, side reactions with the undesired product CO take place [11]. According to Rocha et al [12], the formation of CO as a by-product is especially problematic since even small amounts of CO in the reaction mixture lead to a significant decrease in the performance of a PEMFC. Therefore, intensive research is being conducted to find materials that exhibit catalytic activity as well as high selectivity towards the reaction of methanol steam reforming. A particularly interesting class of materials is that of the perovskite-type oxides. According to Lindenthal et al [13], these materials exhibit the ability to form highly active nanoparticles on their surface under high temperature and reducing conditions. Previous works could demonstrate in a qualitative way, a high level of activity of perovskite-type oxides under the prevailing reaction conditions of MSR [14]. This applies in particular for materials doped with copper and cobalt, making them particularly promising as catalysts for this reaction.

This diploma thesis builds on previous research work that was conducted in the field of MSR using perovskite-type catalysts. The main goal of this work was the establishment of a quantitative analysis of mass spectrometer data as well as the synthesis and investigation of the respective catalysts and their catalytic activity. For this purpose, powder **X**-**R**ay **D**iffraction (XRD) measurements as well as *operando* XRD using Synchrotron radiation was performed in addition to the application of **S**canning **E**lectron

Microscopy (SEM). The assessment of different groups of materials as well as different ratios of doping with cobalt and copper is particularly emphasized. In *Section 1.1*, a short theoretical background regarding the reaction and the thermodynamic situation of the reactions taking place is given. *Section 2* concentrates on the investigated materials and the utilised methods, including the derived formulas for evaluation. In *Section 3* the implementation of the experiment will be explained in more detail, followed by the presentation of the results in *Section 4*, including a comparison of the respective materials. *Section 5* will contain a conclusion of the data obtained. This thesis is concluded with a summary in *Section 6* and a short outlook in *Section 7*.

1.1. Methanol Steam Reforming

In order to better understand the motivation behind this work, a brief theoretical background is presented. This includes the reaction of Methanol Steam Reforming (MSR) and its thermodynamic properties, as well as the complications of conventional catalytic materials for MSR. Furthermore, the material class of perovskites will be discussed, including their properties which make them particularly interesting regarding their use as catalysts.

1.1.1. Reactions and Thermodynamics

As already mentioned in the *previous section*, the reaction of MSR is a promising method for the on-demand production of H_2. There are several reasons why this reaction holds such a potential. For one, methanol does not contain any strong C-C bonds, making it relatively easy to reform. Another advantage is the high proportion of H_2 in reformates (up to 80 %). But the biggest advantage is that methanol exhibits chemical stability and does not need any complex storage situation such as hyperbaric tanks, as pure H_2 does. [11, p. 7016]

For MSR, methanol is reacting with water in a vapour saturated atmosphere, forming the reformates CO_2 and H_2. As stated from Xing et al [15, p. 7017], the ratio of water-to-methanol is of great importance, regarding the occurring side reactions. If the water-to-methanol ratio falls below 1.0 the side reactions listed in Table 1 take place, leading to a decrease in the conversion of methanol to H_2. Above a ratio of 1.0 only the reactions according to Table 2 occur and the reactions of Table 1 don't need to be taken into consideration.

Table 1 – Side Reactions Methanol Steam Reforming
List of side reactions which take place in a methanol-water environment if the ratio of water to methanol falls below 1.0. At higher ratios this reactions need not to be taken into further considerations. Taken from Xing et al [15, p. 7017].

Name of Reaction	Reaction Formula
Dehydration	$2CH_3OH \rightleftharpoons (CH_3)_2O + H_2O$
Methanation	$2CH_3OH \rightleftharpoons CH_4 + 2H_2 + CO_2$
Dehydration	$2CH_3OH \rightleftharpoons CH_4 + CO + H_2 + H_2O$
Decomposition	$3CH_3OH \rightleftharpoons (CH_3)_2O + CO_2 + 3H_2$
Dehydrogenation	$2CH_3OH \rightleftharpoons HCO_2CH_3 + 2H_2$
Formaldehyde synthesis	$CH_3OH \rightleftharpoons CH_2O + H_2$
Carbonation	$CH_3OH \rightleftharpoons C + H_2 + H_2O$

Therefore, a constant ratio of water-to-methanol of at least 1.0 has to be uphold to limit the occurring reaction to MSR, **D**ecomposition of **M**ethanol (DM) and the **W**ater-**G**as-**S**hift (WGS) reaction.

Table 2 – Main Reaction During Methanol Steam Reforming
List of reactions in a methanol-water environment according to their respective reaction enthalpy at a water-methanol ratio above 1.0. Including methanol steam reforming as well as reverse water-gas shift. Taken from Sá et al [16, p. 44].

Name of Reaction	Reaction Formula	Enthalpy ΔH / kJ mol^{-1}
Methanol Steam Reforming	$CH_3OH + H_2O \rightleftharpoons CO_2 + 3\,H_2$	49.7
Decomposition of Methanol	$CH_3OH \rightleftharpoons CO + 2\,H_2$	90.2
Water-Gas Shift	$CO + H_2O \rightleftharpoons CO_2 + H_2$	-41.2

According to the positive enthalpy, MSR is an endothermic reaction. This means that for MSR to take place, energy has to be provided, e.g. via elevated temperatures. Depending on the utilised catalyst, temperatures above 450 °C are necessary for commonly used materials, according to Behrens et al [13, p. 6]. Same as with MSR, DM is an endothermic reaction, with an enthalpy of 90.2 kJ mol^{-1}. It also prefers higher temperatures, leading to the formation of CO and H_2 under the prevailing reaction conditions. In contrast to MSR, the reaction of WGS has a negative reaction enthalpy. This represents an exothermic reaction, meaning that energy is released in form of heat during the

reaction of CO with water. As exothermic reactions are favoured at lower temperatures, an inversion of the reaction equilibrium takes place during the MSR reaction conditions. During the reaction of WGS CO and water are formed via reaction of CO_2 and H_2. [16, p. 44]

1.1.1. Complications of Methanol Steam Reforming

Despite H_2 being the main product in the reactions taking place, the occurring side products, as illustrated in the paragraphs above, have to be taken into account as well. Especially CO is of great importance regarding the deployment of MSR as a possible on-demand production of H_2 for the usage in PEMFC.

The main problem with the formation of CO is the significant performance loss of a PEMFC. The catalytic active anode material of a PEMFC exhibits high affinity towards CO molecules, which bind on the active sites of the platinum-based catalysts and forms strong bonds with its surface. Therefore, the active sites are blocked for any other reactant, lowering the catalytical activity of the material. According to Rocha et al [12, p. 818], a proportion of CO larger than 10 ppm in the reaction mixture is already sufficient for a significant performance loss. This means for the deployment of MSR as a possible on-demand system in combination with PEMFC technology, the formation of CO has to be suppressed. Otherwise, expensive mechanical measures, such as gas purification steps have to be introduced between reaction chamber and FC. [12] [17]

1.1.2. Complications of Established Catalytic Materials

The most common materials for catalysing MSR are $Cu/ZnO/Al_2O_3$ based materials. These catalysts exhibit high catalytic activity towards MSR and low formation rates of CO at lower temperatures. However, their biggest shortcoming is long term stability. Frank et al [18, p. 181] could demonstrate a loss of catalytic activity of 30-40 % after 100 h on stream. This rapid deactivation is caused by several factors. The catalytic activity of this materials is caused by small particles with high surface area of the highly active species of metallic copper. Particles of this species form alloys with the support material, reducing the number of active sites. Additionally, due to the low melting point of copper, thermal sintering of small copper particles takes place under the condition of MSR. The formation of larger particles reduces the surface area of the active species and therefore leads also to a decrease of catalytic activity. [17] [18]

1.2. Perovskite Structures

These restrictions of commercially deployed catalysts pose a challenging search for better suited materials possessing the following properties . First, high catalytic activity is necessary to operate at moderate temperatures. Second, the materials should exhibit high selectivity towards MSR to suppress

the formation of CO. Third, the occurrence of thermal sintering and the possible formation of alloys should be prevented to ensure the long-term stability of the catalyst.

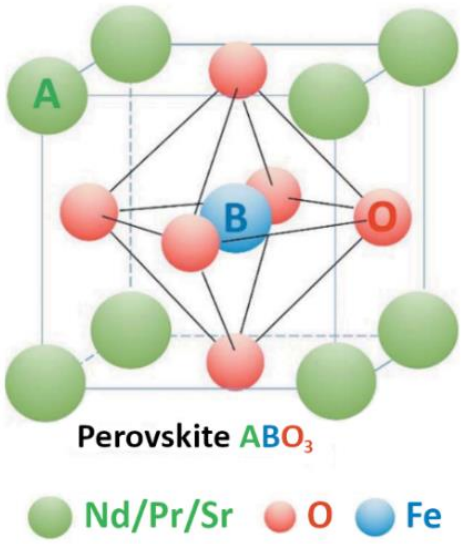

Figure 2 – Perovskite Structure
Illustration of a perovskite-type oxide with the formula ABO_3. In green: A-site cation, in blue: B-site cation and in red: oxygen. Doping of the respective sites is possible. Modified from Lindenthal et al [13].

One promising class of materials are perovskite-typed oxides. Their ability to form highly active nanoparticles on their surface makes them particularly interesting for catalysis. Various studies have already been conducted regarding their catalytic abilities, such as Han et al [19] or Popovic et al [20]. Originally the name perovskite refers to $CaTiO_3$. The class of oxides with a general formula of ABO_3 or A_2BO_4 is nowadays also referred to as perovskites or perovskite-typed oxides. A and B represents cations of variant sizes. Meanwhile oxygen acts as counterion. A and B sites can either be occupied by the same element or by different atoms, which is achieved by doping [21]. But for the crystal structure to be stable certain conditions must be met. As stated by Peña et al [22, pp. 1982–1983], the ratios of the atomic radii hosted by the A- and B-site must not surpass a particular threshold. This threshold, called the Goldschmidt tolerance factor, depends on the used elements and can be calculated according to Equation 1. Besides this threshold, the balance of the total number of charges of a unit cell is also critic for the stability of the crystal structure. Therefore, these criteria must always be considered during the synthesis of perovskite-typed oxides. [23]

$$t = \frac{r_A + r_O}{\sqrt{2} \times (r_B + r_O)} \qquad \text{(Eq. 1)}$$

t ..... *Goldschmidt tolerance factor / -*
r_A ..... *radius of A-site element / Å*
r_B ..... *radius of B-site element / Å*
r_O ..... *radius of oxygen / Å*

The properties of this class of material can easily be modified by doping the A- or B-site with catalytic active metals. Around 90 % of all metallic elements, among them highly active elements such as cobalt and copper, can be accommodated, as long as the requirements as mentioned above are met. Due to

their unique structural features, perovskites also exhibit high thermal stability. This makes them especially interesting for gas phase reactions at high temperatures, like MSR. [21] [23]

1.2.1. Exsolution

The process in which highly active nanoparticles are formed on the surface of the material is called exsolution. According to Islam et al [23, pp. 2–4], nucleation of metal ions on the catalysts surface takes place due to co-segregation of the homogeneous mixed crystal lattice. This leads to the diffusion of exsolvable ions from a depth of up to 100 nm to the surface. There, the metal ions are being reduced to metallic nanoparticles – either as pure metal or as alloys, under a reductive atmosphere, using diluted H_2. It could be demonstrated that these nanoparticles are well pocketed in their surrounding host lattice, submerging about one-third into the surface. Due to this submersion of the particles, these materials exhibit enhanced physiochemical properties compared to materials which solely possess deposited particles on their surface. For example, perovskite-typed oxides display high thermal stability and are being less vulnerable for thermal sintering to occur due to the submersion of the formed nanoparticles. Therefore, these materials are able to preserve their catalytic activity over a longer period of time under the respective reaction conditions. The proposed physical processes occurring during exsolution are diffusion, nucleation, reduction and particle growth. [23] [24]

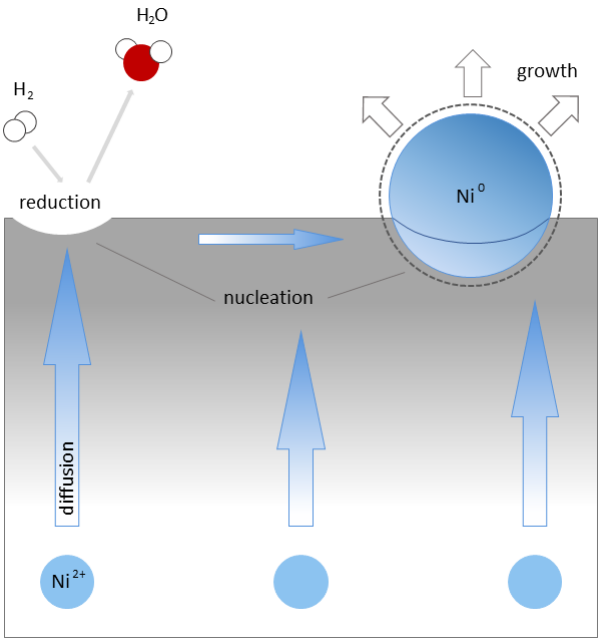

Figure 3 *– Formation of Nanoparticles*
Illustration of the formation of catalytic active nanoparticles on the surface of the material. During the reduction of the material, oxygen vacancies are formed, leading to nucleation. Due to diffusion of exsolvable metal ions, nanoparticle growth takes place on the surface. Modified from Islam et al [23].

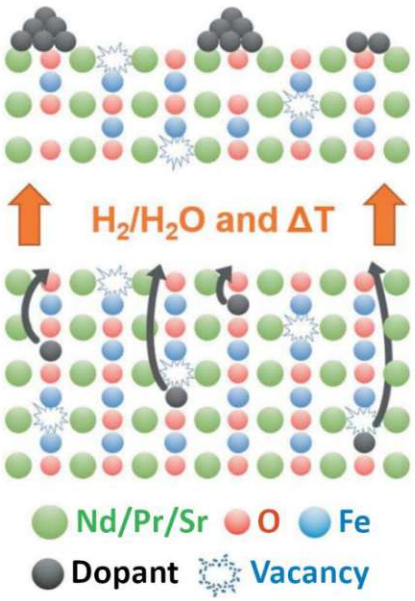

Figure 4 – Exsolution of Nanoparticles
Display of the schematic process of exsolution. Under a reducing atmosphere and high temperatures dopants of the B-site exsolve to the surface of the material. Due to the reductive conditions the dopant-ions are reduced to highly active metallic nanoparticles. Modified from Lindenthal et al [13].

As proposed by Neagu et al [24, pp. 2–4], the process of exsolution is most affected by the occupation of the A- and B-site. As could be demonstrated by the group, the A-site elements are mainly responsible for the stability of the crystal lattice, while the B-site elements exsolve through the bulk and form nanoparticles on the surface. By choosing the appropriate elements for each site, the exsolution behaviour of the respective materials can be modified accordingly. For example, hosting two elements with different atomic radii (e.g.: Nd^{3+} is bigger than the dopant Ca^{2+}), on the A-site leads to a distortion of the crystal lattice, which leads to a destabilization of the structure and promotes the diffusion of B-site ions to the surface. Because of that the stability of the structure is reduced and the diffusion of B-site ions is encouraged. If catalytically active elements are chosen for the doping of the B-site, active nanoparticles are subsequently formed on the surface of the materials. However, it could also be demonstrated that unwanted diffusion of A-site elements is possible to occur due to charge compensation of the crystal structure and a cation size mismatch. Such accumulation of A-site elements on the surface could lead to the suppression of the exsolution of B-site elements and therefore could have harmful effects on catalytic processes. [13] [24]

The proposed driving force of the exsolution process is the formation of oxygen vacancies, as stated by Kwon et al [25, p. 4]. Exposing the materials to high temperatures above 500 °C and reducing conditions (e.g.: diluted H_2), vacancies are formed in the crystal structure. These vacancies cause instability within the structure due to disturbing the stoichiometry of the perovskite. To restore the stoichiometry of the bulk and therefore increase the stability of the structure, spontaneous exsolution of B-site elements occurs. Islam et al [19, p. 4 could demonstrate that this process starts with the formation of pits on the surface with depths of 20-30 nm, in which the exsolved metal ions are accumulated. Due to the reducing atmosphere, these ions are then reduced to metallic nanoparticles, embedded within the surrounding bulk. This process is strongly influenced by the capability of the cations to be transported to the surface through the bulk. The chemical properties of the chosen elements influence the necessary temperature for exsolution to occur. This can be used to control which element forms nanoparticles on the surface of the perovskite. [13] [23] [24]

1.3. Synchrotron Radiation

1.3.1. X-Ray Diffraction

As already mentioned in *section 1*, X-ray diffraction was used during this thesis to study possible changes of the investigated materials under the conditions of MSR. This technique is one of the most important tools for structural elucidation and phase identification of inorganic materials. It is based on the interaction of electromagnetic radiation (X-rays) with electrons in crystal structures. X-rays are scattered by the electron shell. The scattering of coherent radiation by periodic structures is called diffraction, therefore we talk about **X**-**R**ay **D**iffraction (XRD). The periodicity of the atoms in the crystal lattice gives rise to constructive and destructive interference of the diffracted X-rays. This leads to the appearance of pronounced reflection maxima at certain angles, which is known as Bragg's law and can be derived from geometric considerations as depicted in Figure 5. In the case of a polycrystalline sample (e.g. powder diffractograms), this happens randomly and evenly in a conical shape around the primary beam. [26]

$$2 \cdot d_{\mathrm{hkl}} \cdot \sin(q) = n \cdot \lambda \qquad \text{(Eq. 2)}$$

d_{hkl} ..... *lattice plane spacing / nm*
θ ..... *angle of beam / °*
λ ..... *wavelength of incident beam / nm*

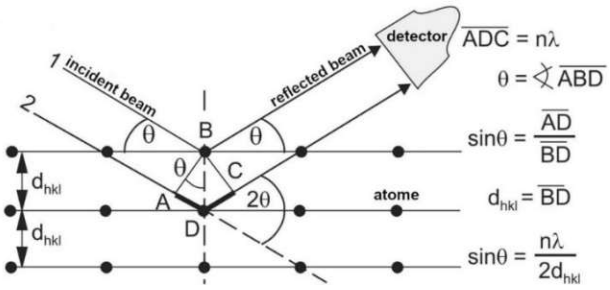

Figure 5 *– Bragg Equation*
Geometric derivation of Bragg's equation. Consideration of the law of reflection under which the angle of the incident ray must be equal to the angle of the exiting ray. In order to obtain a reflection with a measurable intensity, the phase shift caused by the lattice plane spacing d must correspond to an integer multiple of the wavelength of the incident beam. Only in this case will there be constructive interference of the phase-shifted beams, resulting in the Bragg Equation. Modified from Spieß et al [26].

The angles of the reflection maxima are governed by the wavelength of the incident radiation and the lattice parameters of the examined sample. The lower the wavelength of the incident beam, the smaller the observed diffraction angles. In contrast, smaller lattice spacings lead to larger angles. The respective reflection pattern can be used to identify phases within bulk materials. For this intent, the angles of the refraction maxima combined with their relative intensities are compared to X-Ray diffractograms obtained from data bases. [26]

1.1.1. Synchrotron Radiation

To produce the necessary electromagnetic wave (X-ray radiation) several viable radiation sources exist. To describe the differences of these various sources the term of brilliance is used. This term describes the quality of the radiation in terms of number of photos per area and time as can be seen in Equation 3. [26] [27]

$$B = \frac{\Phi}{\Delta\Omega \cdot \frac{\Delta\lambda}{\lambda}} \qquad \text{(Eq. 3)}$$

B ..... *brilliance / Sch*
Φ ..... *photon flux / s^{-1} m^{-2}*
ΔΩ ..... *space angle / rad*
Δλ/λ ..... *wavelength range / -*

Note that the X-ray source brilliance is an invariant quantity, i.e. the brilliance cannot be improved by any optical techniques. For example, if you want to increase the intensity of the incident beam via focusing lenses this comes at the price of higher divergence, which means an unchanged brilliance according to Equation 3. This also holds true for the other way around, if divergency is reduced via collimators a decrease in intensity occurs, again meaning the brilliance of the radiations source is unaffected. [26] [27]

In order to enable *operando* XRD, a high resolution and short measurement periods are required, which can only be achieved by a high brilliance. However, the required brilliance cannot be generated with conventional X-ray tubes, but only with a synchrotron. For example, conventional X-ray tubes display a brilliance between $10^7 – 10^{11}$ photons per second whereas current utilised synchrotron sources exhibit brilliances of up to 10^{21} photons per second. To achieve this high level of brilliance a synchrotron radiation source consists mainly of six components [26] [27]:

(1) **Electron source:** Electrons are formed within an electron gun, typically via thermionic emission via a hot filament. These emitted electrons are then accelerated to roughly 100 MeV using a linear accelerator (LINAC). This electron generating step is repeated periodically due to electron losses within the synchrotron triggered by collisions in the storage ring. [27]

(2) **Booster ring:** For further acceleration after LINAC electrons are injected into the first ring accelerator. Here, the electrons are accelerated to the necessary energy for the main storage ring and are used to maintain the current of the storage ring via regular injection about every two minutes (allowed current drop of storage ring around 1mA). [27]

(3) **Storage Ring:** Keeps electrons on closed path via the use of three types of magnets: dipole magnets, quadrupole magnets and sextupole magnets. The dipole magnet (bending magnet) ensures a closed orbit of the electrons. Quadrupole magnets focus the electron beam to minimize divergency. Lastly, to minimize chromatic aberration caused by focusing the diverging electron beam, sextupole magnets are utilised. [27]

(4) **Insertion device:** In addition to the magnets mentioned above, sitting in the arcs of the storage ring, straight sections are also part of the construction, as depicted in Figure 6. These straight sections are used for generating the highest possible brilliance via insertion devices. [27]

(5) **Radio Frequency Cavities:** Due to the losses of energy caused by the emissions of synchrotron radiation, electrons are not capable to maintain their path through the storage ring on their own. For this reason, radio frequency is used to replenish the lost energy by providing enough extra energy to the electrons every time they pass through the radio frequency cavity. [27]

(6) **Beamline:** To utilise the emitted synchrotron radiation beamlines are located along the axes of the insertion device. They are made up of three main parts: the front end, the optical hutch and the experimental hutch. The main purpose of the front part is to isolate the photon beam from the insertion device coupled with various safety features such as separating different stages of vacuum and monitoring the x-ray and Bremsstrahlung radiation before the optical hutch. In the optical hutch the incident beam can be focused and monochromatized if necessary. Afterwards, the pre-processed beam, adapted to the needs of the end user, is directed into the experimental hutch. There, this high brilliance beam can then be used for high quality measurements. [27]

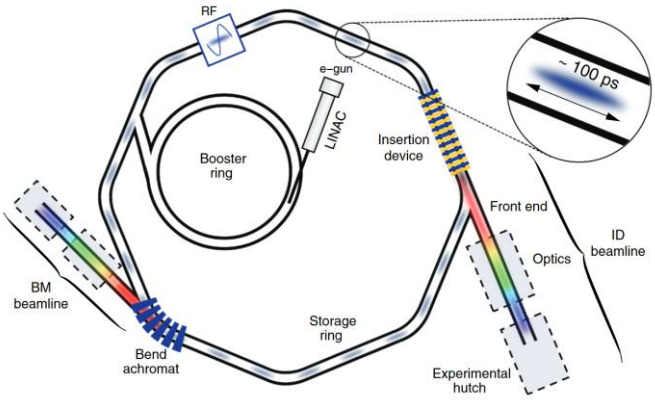

Figure 6 – *Structure of a Synchrotron*
Synchrotron radiation sources consist of six main parts: An electron gun coupled with a linear accelerator to generate the necessary electrons. A booster ring to accelerate the electrons high enough velocity for injection into the storge ring. A storage ring to keep the electrons in an enclosed circle at velocities near the speed of light. Insertion devices to generate the desired synchrotron radiation. Radio frequency cavities to replenish the lost energy of the electrons, and beamlines to utilise the generated radiation for high quality measurements. Taken from Willmott [27]

Due to the ring-shaped arrangement of a synchrotron, electrons are constantly forced to change their direction via bending magnets. From a physical point of view, this change in direction leads to a constant change in the acceleration vector of the electrons. This results in the emission of electromagnetic waves (X-rays, UV light,...) called synchrotron radiation. During this process the velocity of the electrons is kept near the speed of light. [27]

Insertion Devices

This effect of emitting electromagnetic radiation is amplified by the use of insertion devices before the beamlines at which the radiation is utilised. These devices also exploit the fact that changing the direction of the acceleration vector (deflection of the electron beam) creates electromagnetic radiation. The electrons are forced onto an oscillating path in the plane of the storage ring. This is achieved by successive dipoles. In principle, a distinction is made between two variants: wigglers and undulators. The main difference is the type of the emitted radiation. With Wigglers, the electrons are strongly deflected, with high photon energy being obtained. This is achieved by using stronger magnets compared to undulators. The radiation generated in this way has a higher divergence (radiation cone has a larger opening angle). As a result, there is no interference of the radiation, which means that a relatively broad spectrum is achieved. With undulators, on the other hand, the electrons are less deflected. Here, the radiation cone generated displays a significantly smaller opening angle. This leads to the interference of the occurring radiation, whereby a sharper spectrum is achieved. This then results in a higher brilliance. [27]

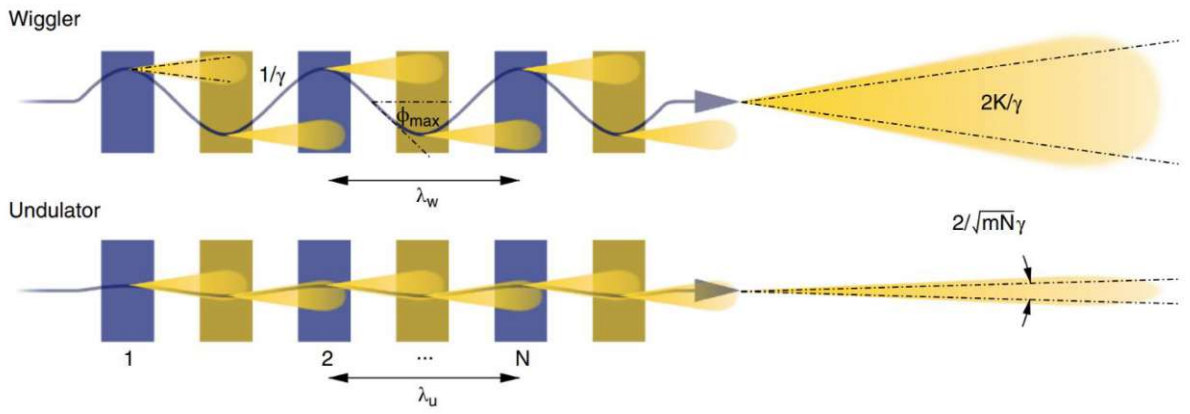

Figure 7 *– Insertion Devises*
There are two possible insertion devices: a Wiggler and an Undulator. The main difference is the type of the emitted radiation. Undulators achieve a smaller divergence compared to a Wiggler, resulting in the interference of the radiation cones and a higher brilliance. This is caused by their difference in the angular deviation they force the electrons to perform. This angular deviation is higher for a Wiggler, resulting in the higher divergence of the electron beam. Taken from Willmott [27]

2. Material and Methods

2.1. Investigated Materials

For this thesis different kinds of perovskite-typed materials were investigated. The basic structures $Nd_{0.6}Ca_{0.4}FeO_3$, $Pr_{0.6}Ca_{0.4}FeO_3$ and $SrTi_{0.7}Fe_{0.3}O_3$ as well as variations of these were examined. For the modification of the basic structure, the B-site was doped with the elements Co and Ni as well as Cu in varying proportions. All investigated materials are listed in Table 3 below, as well as their doping material and their abbreviations used in further succession.

Table 3 – *List of Investigated Catalysts*
The abbreviations listed in the table below will be used in the following sections instead of the proper names of the respective catalysts. The basic structures of the investigated materials are constructed as follows: the A-site is made of Nd, Pr and Sr. The B-site consists of Fe doped with Ca for both Nd and Pr. These structures were modified with Cu and Co as additional dopants of the B-site.

Catalysts	A-site dopant	B-site dopant	Abbreviation
$Nd_{0.6}Ca_{0.4}FeO_3$	Ca	-	NCF
$Nd_{0.6}Ca_{0.4}Fe_{0.9}Co_{0.1}O_3$	Ca	Co	NCF-Co
$Nd_{0.6}Ca_{0.4}Fe_{0.9}Ni_{0.1}O_3$	Ca	Ni	NCF-Ni
$Nd_{0.6}Ca_{0.4}Fe_{0.9}Cu_{0.1}O_3$	Ca	Cu	NCF-Cu10
$Nd_{0.6}Ca_{0.4}Fe_{0.95}Cu_{0.05}O_3$	Ca	Cu	NCF-Cu05
$Nd_{0.6}Ca_{0.4}Fe_{0.95}Cu_{0.03}O_3$	Ca	Cu	NCF-Cu03
$Pr_{0.6}Ca_{0.4}FeO_3$	Ca	Cu	PCF
$Pr_{0.6}Ca_{0.4}Fe_{0.9}Ni_{0.1}O_3$	Ca	Ni	PCF-Ni
$Pr_{0.6}Ca_{0.4}Fe_{0.9}Co_{0.1}O_3$	Ca	Co	PCF-Co
$Pr_{0.6}Ca_{0.4}Fe_{0.9}Cu_{0.1}O_3$	Ca	Cu	PCF-Cu10
$Pr_{0.6}Ca_{0.4}Fe_{0.95}Cu_{0.05}O_3$	Ca	Cu	PCF-Cu05
$Pr_{0.6}Ca_{0.4}Fe_{0.95}Cu_{0.03}O_3$	Ca	Cu	PCF-Cu03

2.2. Experimental Setup

2.2.1. Mass Spectrometry

For the comparability of the catalytic activity of the respective materials a measurement procedure had to be developed. For this, a reactor design was set up, consisting of three main parts: a network of **M**ass **F**low **C**ontrollers (MFC), a horizontal reaction chamber and a mass spectrometer for analysing the reaction progress. As illustrated in Figure 8a the reaction chamber includes an oven, a thermal sensor and a glass capillary. The temperature of the oven could be controlled via a **P**roportional **I**ntegral

Derivative (PID) controller using the thermal sensor. For this, the external software *Eurotherm* was used. The software also enabled the recording of the set and measured temperature over the entire observation period. To investigate the respective materials under the conditions of MSR a network of MFCs was installed. With these, the necessary reaction mixture could be set, depending on the induvial step of the measurement procedure. The catalysts themselves were inserted into the reaction chamber via a capillary made of quartz glass. To hold the material in position during the measurements, quartz glass wool was put on either side of the catalyst bed, as illustrated in Figure 8b.

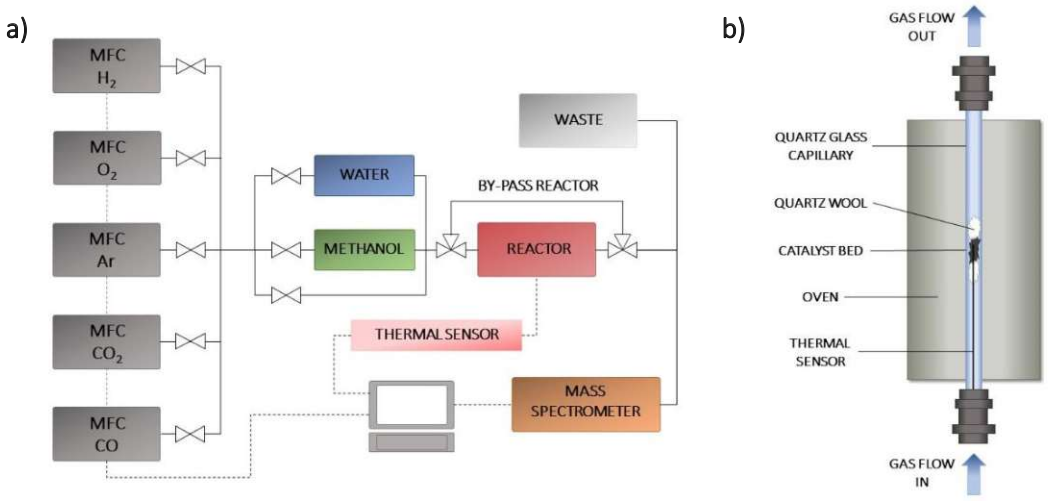

Figure 8 – Reactor Design
***a)** Flowchart of the measurement design. A network of mass flow controllers were used to set the individual gas flows for each step of the measurement procedure. Via by-pass valves the gas flow could be either fed straight into the detector or through the reactor. Additionally, bubblers filled with water and methanol respectively enabled the saturation of the gas phase with one of those components. For the monitoring of the reaction via mass spectrometer, a small portion of the reaction mixture was constantly fed into the MS chamber. All devices were regulated via a central control unit. **b)** Schematic design of the reaction chamber. The catalyst bed is hold into place via quartz wool. The temperature is controlled and recorded via a thermocouple. Modified from Ellersdorfer [28, p. 8].*

A mass spectrometer *Hi Cube* from *Pfeiffer Vacuum* was utilised to observe and evaluate the reaction progress. According to Pfeiffer Vacuum [29], this system incorporates the following parts: an inlet, an ion source, a mass filter, detectors, a vacuum system as well as a data processing unit. Using a combination of a pre-vacuum pump and a rotary vane pump a working pressure of $1.0 – 1.1 \times 10^{-6}$ mbar was assured. This low pressure is required for the ionization of the investigated molecules as stated by the manufacturer [30, p. 3]. The ionization as well as the fragmentation is performed via electron bombardment, using an electrical heated cathode (filament). For the distinction of the individual mass-to-charge (*m/z*) ratios, a quadruple mass filter is applied during the measurement, only recording predefined mass-to-charge ratios (bin mode). The signal intensities of these masses are detected via a

Faraday´s Cup, using a **S**econdary **E**lectron **M**ultiplier (SEM) to enhance the signals, due to the low ion current generated by some of the investigated molecules.

To enable a comparison of the investigated materials, a pre-defined measurement procedure was applied, as illustrated in Figure 9. To guarantee the same starting conditions the respective catalyst was first subjected to an oxygen pre-treatment. Subsequently, a reduction of the respective materials was performed. As stated in *Section 1.2.1.*, catalytic active nanoparticles are formed during this process due to triggering exsolution via high temperatures under reducing conditions. The third step consisted of the evaluation of the baseline value (see *Section 3.2.2.*), followed by the equilibration of the gas phase with the reaction mixture of methanol and water. Afterwards the reaction of MSR was performed using a predefined temperature profile. Finally, reference points for H_2, CO_2 and CO were measured for the quantitative analysis of the recorded data (see *Section 3.2.3.*). Preceding each of the described steps, the system was flushed with argon for several minutes.

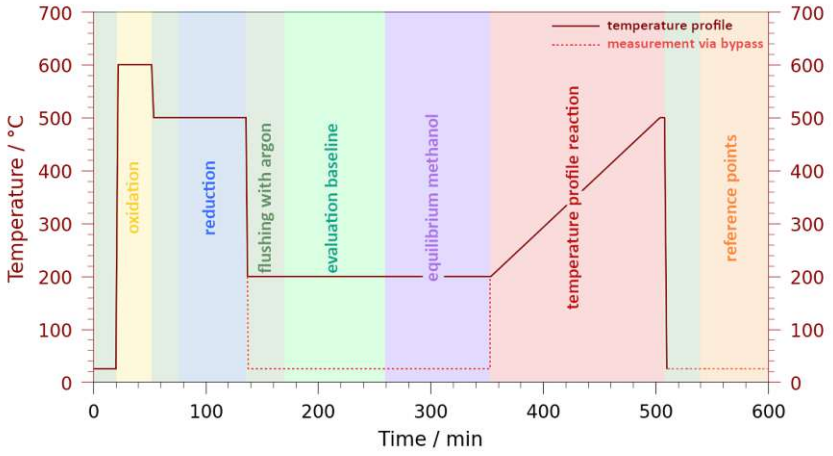

Figure 9 *– Scheme of Measurement*
The system had to be flushed with argon at the beginning of each measurement, as well as after changing the gas composition (green). During the flushing the temperature could be set for the next step if necessary. The first steps consisted of the oxidation via O_2 (yellow), followed by the subsequent reduction with H_2 (blue). Afterwards the baseline of the individual signal could be performed under a constant flow of argon (light green). After the equilibration of the methanol-water atmosphere (violet) a temperature ramp was conducted (red). The procedure was closed with the measurement of reference points (orange).

In the following paragraph these steps of the measuring procedure are being explained in more detail:

- To start the measurement, a constant argon flow of 20 ml min^{-1} was set and the whole system was flushed. Simultaneously, the working pressure was adjusted to 1.0 x 10^{-6} mbar.
- Next the oxygen pre-treatment was performed. For this, a temperature of 600 °C was hold for 30 min while a constant oxygen flow of 20 ml min^{-1} was provided.
- To ensure no oxygen remained afterwards within the system, the pipes were flushed with argon until no oxygen signal could be detected. This was done to prevent any unwanted reaction of

oxygen and H_2 during the process of reduction. Furthermore, the flushing of the system was used to set the necessary temperature for the next step, depending on the investigated catalyst. The respective reduction temperatures are listed in Table 5 in the *Appendix*.

- After reaching the required temperature a constant flow of diluted H_2 of 20 ml min^{-1} was set and passed through the reaction chamber for 60 min.
- Afterwards the system was again flushed with argon and no residue components could be detected the baseline of the individual signals was determined. A more detailed description of the steps necessary for determining the baseline as well as evaluating the reaction period is given in *Section 3.2*.
- During the determination of the baseline the temperature was set to 200 °C for the start of the temperature ramp of the reaction period. This was followed by the equilibration of the reaction components methanol and water in the gas phase. For this purpose, a constant argon flow of 20 ml min^{-1} was passed through a disperser filled with a mixture of methanol and water in a 1:4 ratio (volumetric). The disperser was kept at a constant temperature of 20 °C. The ratio of these two fluids was chosen so that their ratio in the gas phase equalled 1.0. The equilibration of the gas phase was performed using the by-pass.
- Only after achieving a constant signal of methanol was the reaction mixture passed through the reaction chamber. During the reaction period the catalyst was subjected to a temperature ramp ranging from 200 °C to 500 °C with a heating rate of 2 °C min^{-1}. During this observation period the set as well as the measured temperature was recorded and used as a control mechanism for the reaction and possible phenomena taking placing.

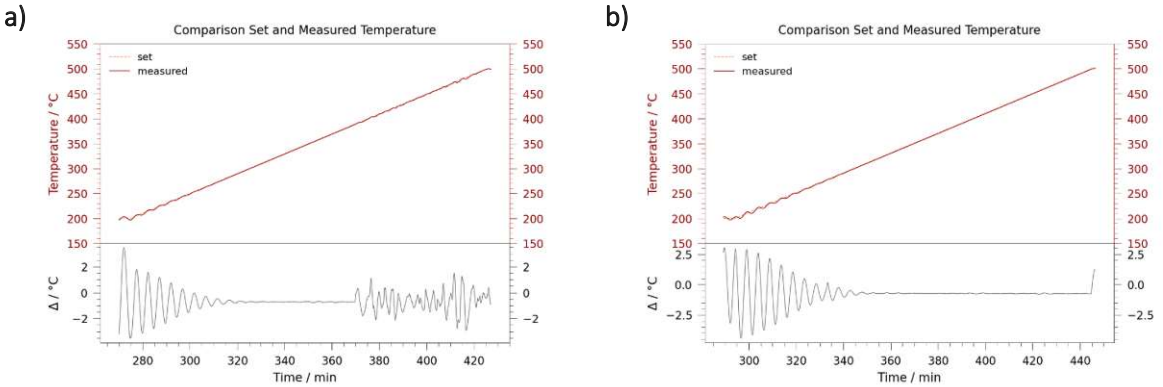

Figure 10 *– Temperature Control*

Illustration of the temperature control during the reaction period. After a transient phase at the beginning of the temperature ramp, the difference between the measured and the set temperature should remain stable. ***a)*** *Illustration of a discrepancy at higher temperatures.* ***b)*** *Depiction of a regular reaction period, demonstrating the transient phase at the beginning and a stable temperature difference at the end of the temperature ramp. This was calibrated in a temperature range of around 400°C, which makes temperature control difficult below this range.*

As illustrated in Figure 10, the differences between the set and the measured temperature was recorded over the observation period. This was done to corelate possible phenomena occurring in the catalyst data with deviations of the actual temperature of the reactor. After an initial transient phase at the beginning of the temperature ramp, the temperature difference should remain stable over the rest of the reaction period as in Figure 10b.

2.2.2. Scanning Electron Microscopy

To investigate the surface of our catalysts **s**canning **e**lectron **m**icroscopy (SEM) experiments were performed at DESY with a FEI Nova Nano SEM 450 instrument (*FEI Company, Hillsboro, OR, USA*). For detection an Everhart-Thornley detector (ETD) was utilised. The recording of the images was done using an acceleration voltage of 5 kV and the utilisation of secondary electrons.

2.2.3. X-Ray Diffraction

To verify the phase purity after synthesis of the respective catalysts as well as phase changes after the reaction, powder XRD measurements were performed. For this, a PANalytical X'Pert Pro diffractometer (*Malvern Panalytical, Malvern, UK*) in Bragg–Brentano geometry with an X'Celerator linear detector (*Malvern Panalytical, Malvern, UK*) was utilised with a mirror for the separation of the Cu $K_{\alpha1}$ and Cu $K_{\alpha2}$ radiation.

For the investigation of possible phase changes during the reaction *operando* powder XRD measurements were carried out. These measurements were performed on beamline P02.1 at DESY (*Deutsches Elektronen-Syntrochtron, Hamburg, Germany*) in transmission geometry, using an energy of 60 keV (0.207 Å). For the recording, an area detector was utilised.

The set up used for the *operando* investigation of the respective catalysts is similar to the reactor design described in *section 2.2.1.* and can be seen in Figure 11. The design consists of a mass flow control unit, a quartz capillary with a diameter of 0.7 mm, mounted between two resistance heating wires, and an MS unit to check the out flow of the capillary. The whole set up could be controlled via an external computer unit.

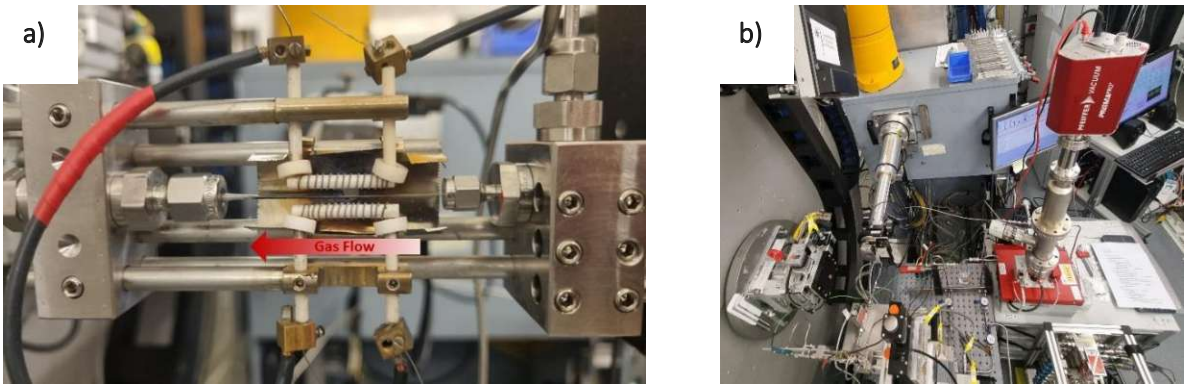

Figure 11 – Measurement Set Up for Operando XRD
a) Illustion of the utilised measuring unit containing the capillary, a heating wires and a thermocouple to control the temperature within the unit. b) Depiction of the whole set up including the MS, the external computer unit as well as the gas mixture unit and the radiation outlet.

For the purposes of the *operando* measurements no quantification of the MS data was performed. Therefore, the measurement procedure could be simplified as follows. No determination of baseline values was necessary. Additionally, the measurement of reference points after the temperature ramp could be omitted. Therefore, the measurement procedure consisted of an oxidation and reduction phase, followed by the equilibration of the gas phase and a temperature ramp from 200 °C to 500 °C. XRD data was collected every three seconds over the entire observation period.

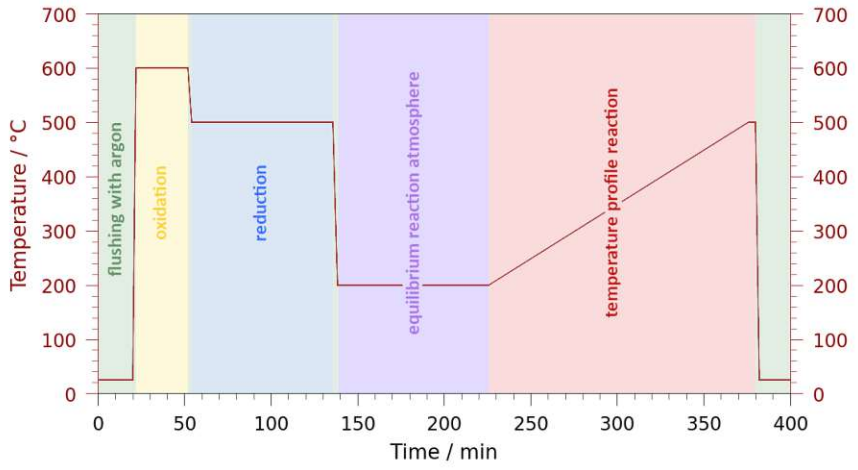

Figure 12 – Scheme of Measurement at Beamline P2.01
At the beginning of each measurement, as well as after changing the gas composition the system was flushed with Ar. During the flushing the temperature could be set for the next step if necessary. No evaluation of the baseline of the signal was necessary. The equilibrium of the methanol-water atmosphere was done at 200°C. After one hour of equilibration time the temperature ramp, ranging from 200 °C to 500 °C, was started. Over the entire measurement period XRD data was collected.

2.3. Data Evaluation Methods

2.3.1. Mass Spectrometer

Using the acquired quantitative data of the mass spectrometer various calculations could be performed, including the yields of H_2, the conversion of methanol, the specific activity of the catalyst as well as its selectivity. All calculations performed during this work were done using an automated Python script, which can be found in the *Appendix*.

2.3.1.1. Yield of H_2 and CO_2

The reaction formula of MSR, as depicted in Table 1 (*Section 1.1.1.*), illustrates that for one mole of methanol three moles of H_2 are produced. This correlation is used for determining the yield of H_2 over the observation period. Measuring the amount of methanol via by-pass equals a H_2 concentration three times larger at 100 % yield, since every mole of methanol is theoretically converted into thrice the molar amount of H_2. By measuring the molar amount of methanol via by-pass before the start of the temperature ramp and the subsequent recording of the H_2 amount during the reaction period, it is possible to calculate the yield of H_2 according to Equation 4 at any point in time.

$$Y_{H_2} = \frac{n_{H_2}}{3 \cdot n_{MeOH}} \cdot 100\% \qquad \text{(Eq. 4)}$$

Y_{H2} ..... *yield of H_2 / %*
n_{H2} ..... *amount of H_2 in the gas phase / mol-%*
n_{MeOH} ..... *amount of methanol in the gas phase / mol-%*

Like for H_2, the yield of CO_2 can be calculated via the ratio of the converted methanol to CO_2. However as illustrated in Table 1, one mole of methanol results also in only one mole of CO_2. This means that the methanol concentration measured in the by-pass stream corresponds to a CO_2 concentration at 100 % yield. Therefore, to calculate the yield of CO_2, had to be adjusted, according to Equation 5.

$$Y_{CO_2} = \frac{n_{CO_2}}{n_{MeOH}} \cdot 100 \qquad \text{(Eq. 5)}$$

Y_{CO2} ..... *yield of CO_2 / %*
n_{CO2} ..... *amount of CO_2 in the gas phase / mol-%*
n_{MeOH} ..... *amount of methanol in the gas phase measured via by-pass valve / mol-%*

2.3.1.2. Conversion of Methanol

To determine the conversion of methanol two sets of information were needed. The first one consisted of the amount of methanol measured during the equilibration of the reaction atmosphere via by-pass.

The second one was the amount of methanol in the gas phase at each point in time. These information was then used, utilising Equation 6, to calculate the conversion of methanol over the entire observation period.

$$X_{\mathrm{MeOH}} = 1 - \frac{n_{\mathrm{MeOH}}}{n_{\mathrm{MeOH,0}}} \cdot 100 \qquad \text{(Eq. 6)}$$

X_{MeOH} ..... *conversion of methanol / %*
n_{MeOH} ..... *amount of methanol in the gas phase at a given time / mol-%*
$n_{MeOH,0}$ ..... *amount of methanol in the gas phase measured via by-pass valve / mol-%*

2.3.1.3. Specific Activity

Using Equations 7 and 8 the specific activity of the respective catalysts could be calculated. For this, the varying composition of the gas phase is first taken into consideration. In Equation 7 the gas flow of methanol $\dot{V}(X_{MeOH})$ after reacting with water is calculated over the entire observation period. This is done by correlating the gas flow $\dot{V}(0)$ as set via MFC with the amount of the limiting reactant methanol and the amount of the product CO_2 as reference molecule, as presented below.

$$\dot{V}(X_{\mathrm{MeOH}}) = \dot{V}(0) + \varepsilon \cdot \dot{V}(0) \cdot \frac{n_{\mathrm{MeOH}}}{n_{\mathrm{MeOH}} + n_{\mathrm{CO_2}}} \cdot x_{\mathrm{MeOH}} \cdot Z \qquad \text{(Eq. 7)}$$

$\dot{V}(X_{MeOH})$ ..... *gas flow after reaction / $m^3\ s^{-1}$*
$\dot{V}(0)$ ..... *gas flow before reaction as set by MFC / $m^3\ s^{-1}$*
ε ..... *volume correction factor / -, $\varepsilon = 1$*
n_{MeOH} ..... *amount MeOH / mol-%*
n_{CO2} ..... *amount CO_2 / mol-%*
x_{MeOH} ..... *molar ratio methanol / -, limiting component*
Z ..... *number of educts / -, $Z = 2$*

The calculated values of the varying gas flow of methanol can then be used in a second step to determine the specific activity of the respective catalysts. For this, the respective surface of each catalyst, as listed in Table 5 in the *Appendix* as well as the amount of CO_2 is needed, according to Equation 4. The specific activity can then be calculated via the ratio of this components.

$$specific\ activity = \frac{n_{CO_2} \cdot \dot{V}(X_{MeOH})}{S \cdot V_N} \quad \text{(Eq. 8)}$$

specific activity ..... *specific activity / mol s^{-1} m^{-2}*
n_{CO2} ..... *amount of CO_2 / mol-%*
$\dot{V}(n_{MeOH})$ ..... *gas flow after reaction / m^3 s^{-1}*
S ..... *absolute surface of the respective catalyst / m^2*
V_N ..... *norm volume / m^3 mol^{-1}, V_N = 0.0224 m^3 mol^{-1}*

2.3.1.4. Selectivity

The selectivity of the investigated catalysts during the reaction conditions can be calculated using the amounts of the respective products. For this, the summed amount of the desired products H_2 and CO_2 is divided by the summed amount of all products generated which can be seen in the equation below.

$$selectivity = \frac{\sum n_{desired}}{\sum n} \cdot 100 \quad \text{(Eq. 9)}$$

Selectivity ..... *selectivity / %*
$n_{desired}$ ..... *amount of desired product / mol-%*
n ..... *amount of any product / mol-%*

3. Experimental Part

3.1. Sample Preparation

3.1.1. Synthesis

The synthesis of the individual samples was done in several steps according to the Pechini method. [31] Stoichiometric amounts of the specific metal or its appropriate salt were weighted in accordingly and dissolved in water respectively. If necessary small amounts of HNO_3 were added to the solution until the solid material was fully dissolved. For this purpose, the following compounds were used: Nd_2O_3 (99.999%, Alfa Aesar, Haverhill, MA, USA), $CaCO_3$ (99.999%, Alfa Aesar, Haverhill, MA, USA), Fe (99.99%, Sigma-Aldrich, St. Louis, MO, USA), $Pr_2(CO_3)_3 \times 8H_2O$ (99.995%, Sigma-Aldrich, St. Louis, MO, USA), Cu (99.995%, Sigma-Aldrich, St. Louis, MO, USA), $Ni(NO_3)_2 \times 6H_2O$ (99.995%, Sigma-Aldrich, St. Louis, MO, USA) and $Co(NO_3)_2 \times 6H_2O$ (99.995%, Sigma-Aldrich, St. Louis, MO, USA). These solutions were mixed together with the addition of citric acid (99.9998% trace metals pure, Fluka, Honeywell International, Charlotte, NC, USA) in a molar ratio of 1.2 with respect to the cations to form cation complexes. The resulting mixture was evaporated and the dry residue heated until it ignited. After complete incineration of the residue, it was calcined at 800 °C for three hours, ramping the furnace up to the desired temperature at 2 °C min^{-1}. For a better characterisation the material was grinded using a mortar to get a homogenous powder. To make sure the resulting perovskite-typed oxides exhibit the required structure and phase purity, XRD analysis was performed after each synthesis.

3.1.2. Methanol Water Mixture

For the quantitative analysis of the reaction mixture, including methanol, the exact composition of the gas phase has to be determined. Furthermore, as mentioned in section 1.1.1., a molar ratio of 1:1 for methanol and water in the reaction atmosphere has to be maintained. This was done using a set volumetric ratio of the liquid components water and methanol. However, since this mixture exhibits non-ideal behaviour, as demonstrated by Silva et al [32], the law of Raoult could not be used for determining the necessary volumetric ratio. Therefore, vapour-liquid equilibria diagrams calculated by Hartono et al [33] were utilised. With them, the molar ratio of the methanol-water mixture was concluded to be 1:10 as depicted in Figure 12, leading to a volumetric ratio of 1:4.

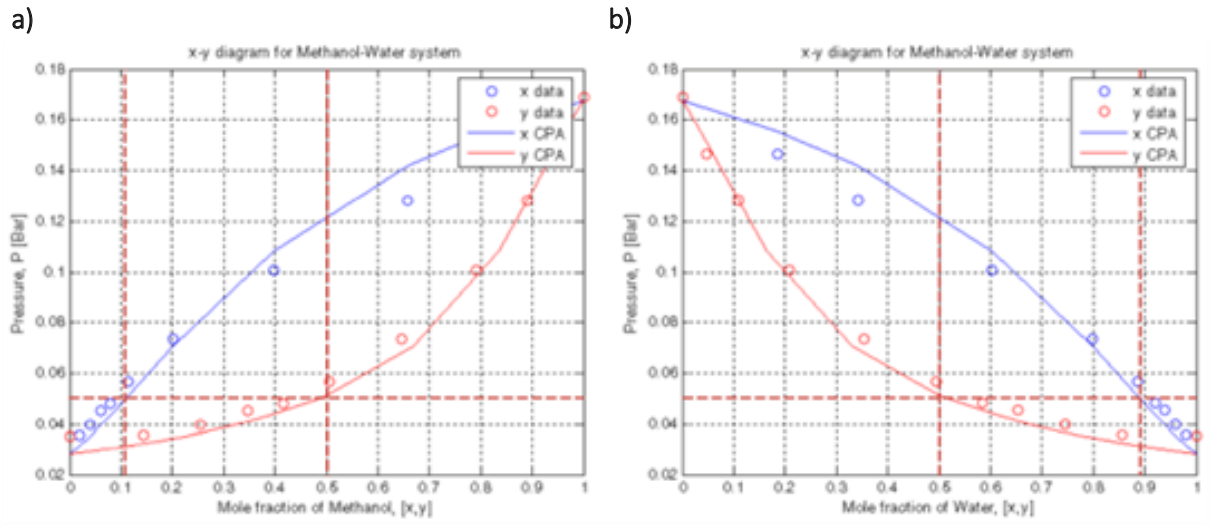

Figure 13 – Vapour-Liquid Equilibrium of a Methanol-Water Mixture
Illustration of a vapour-liquid equilibrium diagram of a methanol-water system. In this context X (blue) is the molar fraction of the liquid phase and Y (red) that of the gas phase ***a)*** *For a methanol-water ratio of 1:1 in the gas phase the mole fraction of methanol in the liquid phase needs to be 0.1.* ***b)*** *Demonstration of the necessary mole fraction of 0.9 for water in the liquid phase for the required mole ratio in the gas phase. Diagrams adapted from Hartono et al [33].*

3.2. Catalytic Measurements using Mass Spectrometry

As already mentioned in *Section 2.1.*, different kinds of perovskites were investigated regarding their ability for catalysing the reaction of MSR. The individual measurement parameters of the respective catalysts are listed in Table 6 in the *Appendix*. including the deployed mass as well as their applied reduction temperature. For each catalyst their relative surface, and the ideal temperature for the reduction treatment was determined in separate investigations. The reaction procedure as described in *Section 2.2.1.* was performed on all materials.

In this thesis a method for the quantitative analysis of catalytic information was implemented. As mentioned in previous sections, the reaction environment of MSR consists mainly of the components methanol and water. Due to the water saturated gas atmosphere a quantification of the reaction gases proved to be challenging. A standard procedure of quantitative analysis of gas streams would be the implementation of a **G**as **C**hromatography (GC). This form of analysis is easily calibrated and exhibits only a small error of results. But unfortunately, it is not suited for the reaction conditions presented by MSR. Therefore, a calibration strategy for a **M**ass **S**pectrometer (MS) had to be applied to be able to compare the different investigated materials, regarding their catalytic activity. The implementation of such a procedure consisted of several steps which will be explained in more detail in the following sections. The execution of the evaluation of each step was done automatically via an implemented Python script.

3.2.1. Normalisation of Raw Data

As described in *Section 2.2.1.*, a working pressure of 1.0 x 10^{-6} mbar was set at the beginning of the procedure. However, it was not possible to maintain a constant pressure due to slight fluctuations over the measurement period. Furthermore, it could be observed that the signal intensities of the respective measurements displayed a high dependency on the current working pressure. Different measurements with increasing working pressure were conducted to check for any correlation between pressure and signal intensity. As depicted in Figure 14a, a constant increase in signal intensity could be observed with higher pressure. Due to this correlation between pressure and signal intensity, the comparability of different measurement runs suffered. Therefore, it was necessary to normalise the raw data. For this, the individual signal intensities were divided by the recorded pressure within the analysis chamber at each point in time.

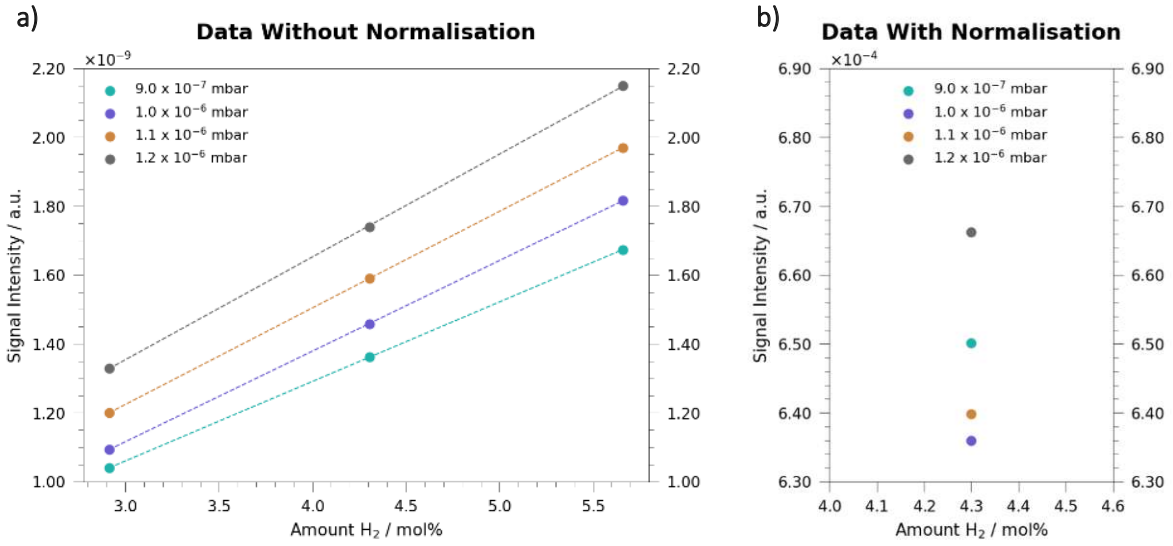

Figure 14 *– Pressure Dependency*

Display of the pressure dependency of the MS signal for hydrogen. ***a)*** *With increasing working pressure higher signal intensity can be observed for the individual signals. Comparison of the distribution of the signal intensities before* ***a)*** *and after* ***b)*** *normalisation of the raw data using the prevalent pressure. After normalisation of the data a random distribution of signal intensities can be observed with no correlation to the working pressure.*

After normalising the data two effects could be observed. On one hand, the differences between the individual measurements now displayed a random distribution without any correlation to the prevalent pressure as highlighted in Figure 14. On the other hand a reduced **r**elative **s**tandard **d**eviation (RSD) of the data points could be observed. Without any normalisation the data points exhibit a RSD of 10 %, after the normalisation process a RSD of 2 % could be found. This normalization enables a more precise assignment of the signal intensity to a defined concentration.

```
## Normalisation of Signals using Working Pressure ----------------------------

# to avoid pressure dependency of the signal intensities
# ratio of individual signal and recorded pressure
# for H2, CO2, CO and MeoOH

def program normalisation

        for all signals:

                norm_signal = signal/pressure

end program normalisation
```

Figure 15 – Implementation of the Normalisation Process
Due to the pressure dependency of the individual signals a normalisation of the raw data was necessary. For this the recorded pressure over the observation period was used. For each signal (H_2, CO_2, CO and MeOH) the ratio of the signal and the recorded pressure was calculated.

3.2.2. Baseline Correction

The next step consisted again of the correction of the data. The system displayed a constant signal intensity of the respective *m/z* ratios, despite the absence of any of these components in the gas atmosphere. This effect could be demonstrated for all measurements performed. It was therefore concluded that each signal displayed a particular baseline which had to be subtracted from the raw data to not overestimate the respective intensities. The baselines of the individual signals are system dependent and are based on two main contributors. The first one is the detector drift, which represents a shift of the signals from zero. The second one is the chemical noise, which corresponds to the noise level of each spectrum after subtraction of the detector drift. [34]

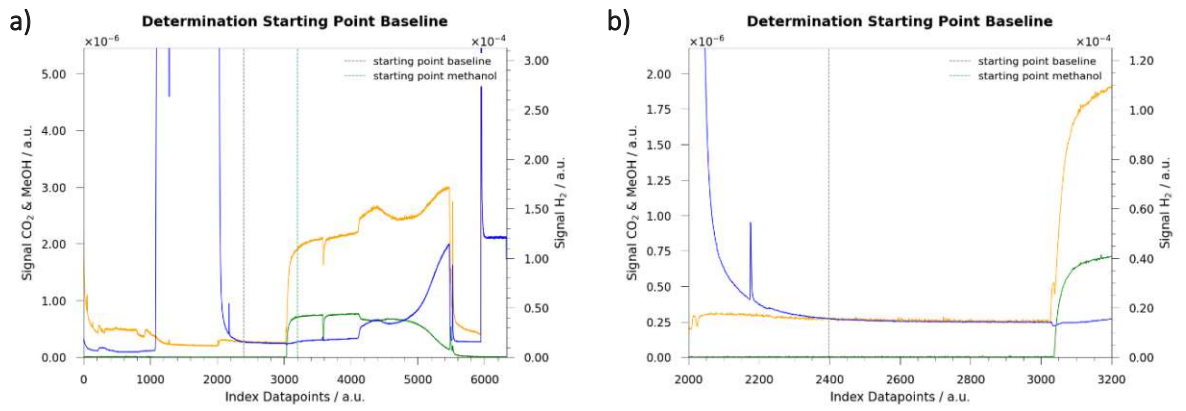

Figure 16 – Baseline Correction
*Display of measurement procedure. **a)** Illustration of complete measurement run displaying the signals for hydrogen, methanol and CO_2. The signal development over the pre-treatments as well as the evaluation and reaction period can be observed. **b)** Range of data point for calculating the baseline value. For the determination of the start of the baseline the point at which the hydrogen signal remained stable had to be found. This was done automatically. The found starting point is indicated via the dashed, grey line.*

```
## Baseline Correction of Normalised Data ------------------------------------

# calculation of baseline of individual signals
# H2 signal as reference signal for determination of starting point
# evaluation baseline after reduction period

def program baseline_correction

# search of start of the baseline necessary
# stable H2 signal after the reduction period indicated start of baseline
# search window adaptable
# threshold for determination adaptable

        for signal_H2:

                find stable signal via standard deviation of search window

                return found index

# found index used as starting point for calculation of baseline
# same starting index used for all signals

        for all signals:

                calculate mean value of baseline starting from found index

end program baseline_correction
```

Figure 17 – Implementation of the Baseline Correction
The correction of the raw data via the baseline values consists of two steps. The first is the determination of the starting point of the baseline calculation. For this, the signal of H_2 is used as a reference to find a stable signal after the reduction period which indicates the start of the baselines. The found index is used for all signals as the starting point for the calculation of the mean value of the individual baseline.

However, the value of the individual baseline of the different *m/z* ratios was not consistent throughout the different measurements and therefore had to be calculated for each evaluation. This was done by flushing the system with argon and simultaneously measuring a constant signal (baseline) of the individual *m/z* ratios. It could also be demonstrated that the value of the baseline correlated with the state of the measurement system.

For example, it was observed that the baseline of H_2 was elevated after the reduction period. To reduce the influence of any correlating effects, the evaluation of the individual baselines of the signals was performed just before the reaction period. For this, the starting point of a stable signal had to be determined due to a steady decline of the signals after flushing the system with argon, as illustrated in Figure 16. This was done automatically, via comparison of the standard deviation of a predefined search window and a threshold value while scanning over the examined range of data points. The range of the window was set to 170 datapoints. The threshold for determining the starting point were obtained empirically. Due to the high sensitivity of the H_2 signal towards changes in intensity, it was selected as a reference for deriving the starting point.

With the obtained start of the evaluation the mean value of the baseline was calculated, eliminating all possible outliers in the process. For this, a set of upper and lower limits was set for each *m/z* ratio. These limits were permitted deviations from the previously obtained value of the starting point of the respective signals. Each datapoint was checked, whether it could be found within these limitations or not. The set of limits were also obtained empirically. As the termination condition for the calculation of the mean value, the finding of a succession of several outliers in the CO signal was chosen, indicating the beginning of the next step of the measurement procedure. The obtained baseline values of the respective signals were subtracted afterwards to correct the signal intensities accordingly. The settings necessary for the execution of the script are listed in Table 8 in the *Appendix*.

3.2.3. Calibration of H_2, CO_2 and CO

After these pre-processing steps of normalisation and baseline correction, the quantitative analysis of the data could be executed. For this, an external calibration of the reaction gases was performed. The calibration of the gases H_2, CO_2 and CO was done separately. To achieve the necessary amount of reactant in the gas atmosphere the gases were diluted with argon to maintain a constant flow rate of 50 ml min^{-1}. The lower limit of the calibration range was restricted by the technical limitations of the mass flows. A list of the individual calibration points of the respective gases can be found in Table 10 in the *Appendix*.

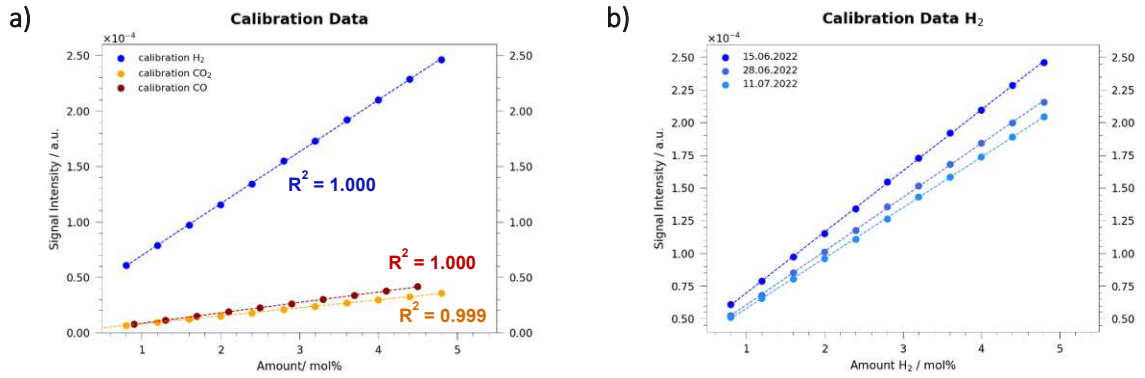

Figure 18 *– Calibration of H_2, CO_2 and CO*
Behaviour of components during calibration. ***a)*** *Illustration of regression line of the reactants H_2, CO_2 and CO. The performed calibrations exhibit high linearity respectively.* ***b)*** *Display of the development of the calibration line of hydrogen. The gradient of the regression line is decreasing over time while the axis intercept remains constant.*

Each calibration of the components exhibited high linearity as illustrated in Figure 18a. However, it could be observed that the gradient of the calibration slope decreased over time, while the axial intercept remained approximately constant. This time dependent change of the calibration parameter proved to be challenging for the application of the calibration. Since only the gradient was subject to a change, it was concluded that the actual slope of the calibration line consisted of the measured gradient and an

additional correction factor. Therefore, reference points with defined proportions of the respective gases (H_2: 1.4 mol%, CO_2: 1.2 mol%, CO: 1.45 mol%) were recorded with each measurement run. With these, the correction factor of the gradient could be calculated according to Equation 11. The correction of the calibration parameter was performed for each measurement.

$$y_i = f \cdot k \cdot x_\mathrm{i} + d \qquad \text{(Eq. 10)}$$

$$f = \frac{y_\mathrm{i} - d}{k \cdot x_\mathrm{i}} \qquad \text{(Eq. 11)}$$

*f*_____correction factor / -
*y_i*_____signal intensity of component i / a.u.
*x_i*_____amount of component i / mol%
*d*_____axial intercept of calibration line / a.u.
*k*_____slope of calibration lline / -

After conducting several measurements, it could be observed that the signal intensities of the reference points are declining steadily, despite the same conditions for each component throughout the different measurement runs, as illustrated in Figure 19. This behaviour could be the result of a reduced sensibility and an increasing saturation of the detector. The development of the signal intensities of the reference points proved the necessity of evaluating the reference points in each measurement run.

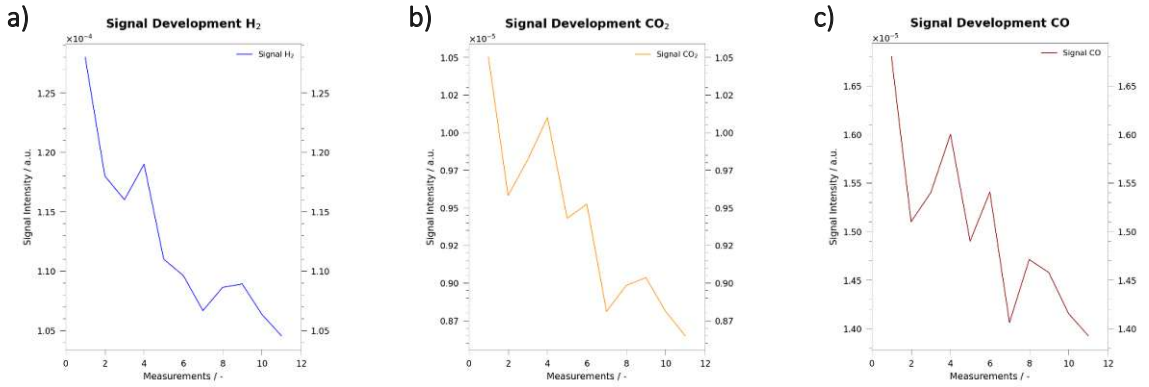

Figure 19 *– Decline of Signal Intensity*
A decrease in signal intensity of the individual reference points could be observed for all components investigated. The signals of ***a)*** *H_2,* ***b)*** *CO_2 and* ***c)*** *CO exhibit a steady decline in intensity. The measurement conditions, such as the set flow of the individual gas was kept constant. For all measurements the total flow was set to 50 ml min^{-1}.*

3.2.4. Calibration of Methanol

As with the reactants H_2, CO_2 and CO, an external calibration for methanol (MeOH) was performed. For this, the reaction atmosphere during MSR with a molar ratio of water and methanol of 1:1 was set and diluted with argon in varying degrees. As already mentioned in *Section 3.1.2.*, this was done with a methanol-water mixture.

For the calibration of the methanol signal, knowledge of the exact proportion of methanol in the gas atmosphere is necessary. Dobruskin [35] could demonstrate a correlation between the enthalpy of evaporation, the set temperature, the respective partial pressure and the proportion of the components. This correlation, expressed in Equation 12, could be used to determine the exact proportion of methanol in the gas phase at a given operating temperature.

$$\Delta(\Delta H) = -R \cdot T \cdot \ln\left(\frac{p}{p_s}\right) \qquad \text{(Eq. 12)}$$

Δ(ΔH) ..... *enthalpy of evaporation / J*
T ..... *temperature which correlates with the respective partial pressure / K*
R ..... *gas constant / J mol^{-1} K^{-1}, R = 8.314 J mol^{-1} K^{-1}*
p ..... *vapour pressure of pure methanol at T / bar*
p_s ..... *partial pressure of methanol at T / bar*

For the calculations a total pressure of 1.013 bar of the reaction gas was assumed with a molar ratio of methanol to water in the reaction mixture of 1:1, as mentioned in the paragraphs above. To modify the amount of methanol, different temperatures for the saturation of the gas phase were applied for each calibration point. The proportion of methanol for each step could then be calculated and subsequently correlated to the measured MS signal. A summary of the set parameters for the calibration can be found in Table 9 in the *Appendix*.

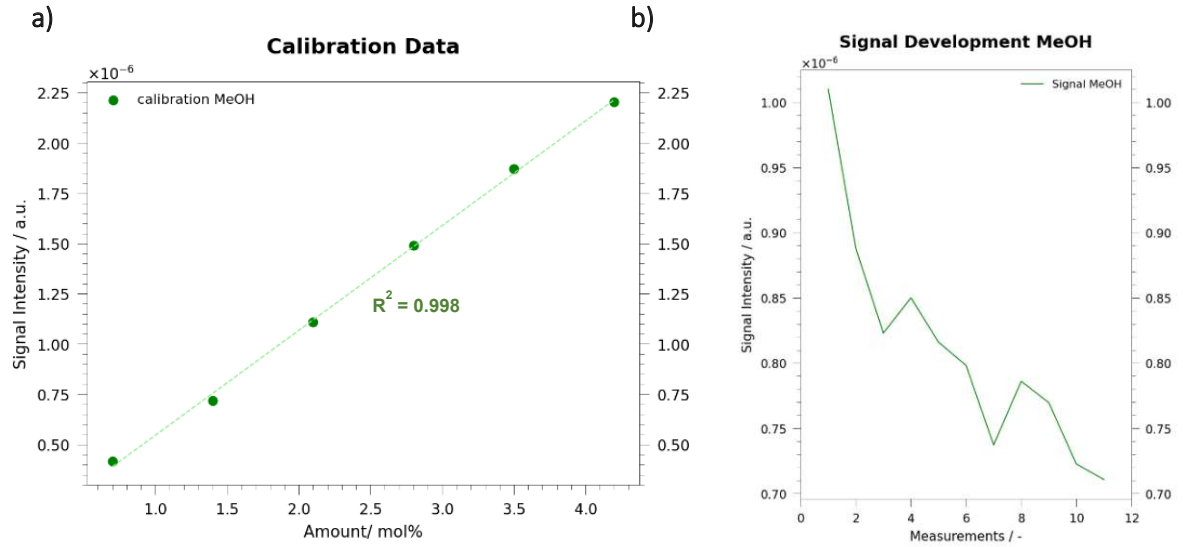

Figure 20 *– Calibration Data of Methanol*
Illustration of the calibration of methanol. ***a)*** *The regression line of methanol exhibits high linearity within the chosen working parameters.* ***b)*** *But, like with the signals of H_2, CO_2 and CO, the signal of methanol at the reference point (2.1 mol%) is declining over time. For this reason, the correction factor for the calibration has to be calculated similar to the other reaction components for each measurement run to counteract any influence on the signals.*

As depicted in Figure 20a, the calibration of methanol displayed high linearity. But, similar to the calibration of H_2, CO_2 and CO, a decrease in the gradient of the calibration slope was observed. Therefore, a correction factor of the slope was calculated according to Equation 11, using the acquired data during the equilibration of the methanol signal of the measurement procedure. As illustrated in Figure 20b, the signal intensity during the equilibrium phase (2.1 mol%) is declining, similar to the signal intensities of the reference points for H_2, CO_2 and CO. For this reason, a correction of the calibration parameters needed to be performed for each measurement.

3.2.5. Fragmentation Pattern

During the calibration of the reaction component methanol, it could be observed that the signal of the *m/z* ratios 44 (CO_2), 28 (CO) and 2 (H_2) were elevated. These elevated signals are caused by fragments of the parent molecule MeOH. During the ionisation of the reaction components via electron bombardment, bonds of the parent molecule break, forming fragments with possible *m/z* ratios of 2 and 28. At the same time the formed fragments can accumulate to bigger ions resulting in fragments with *m/z* ratios of 44. The amount of these measurable fragments correlates with the proportion of methanol in the reaction gas, forming a specific fragmentation pattern.

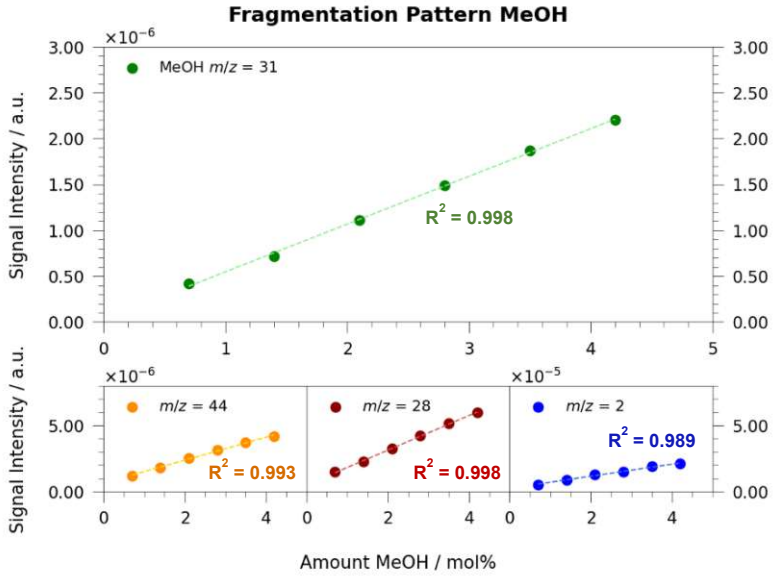

Figure 21 – Fragmentation Pattern of Methanol
Illustration of the fragmentation of the parent molecule methanol. Due to the electron bombardment during the ionisation process the molecule can split into neutral or charged fragments with various m/z ratios, e.g. 2 (H_2) or 28 (CO). These fragments can also collide and form larger molecules, again either as ions or as neutral (and therefore undetected particles). Display of the correlation between the proportion of methanol in the gas phase and the amount of fragments of m/z = 44 (CO_2), m/z = 28 (CO) and m/z = 2 (H_2).

In Figure 21 the fragmentation pattern of methanol with various proportions of methanol is illustrated. As could be demonstrated, the fragmentation of the parent molecule exhibits a linear behaviour with increasing amount of methanol. The correlation between the amount of methanol and the signal intensity of the respective fragments could be used to determine a correction of the individual signals (H_2, CO_2 and CO) during the measurement procedure. As displayed in Figure 22, the component CO_2, like methanol, also exhibits a specific fragmentation pattern leading to the elevation of the signal intensity of the *m/z* ration of 28. Same as with methanol, the correlation between signal intensity and amount of CO_2 were used to correct the signal of CO during the measurement procedure of MSR.

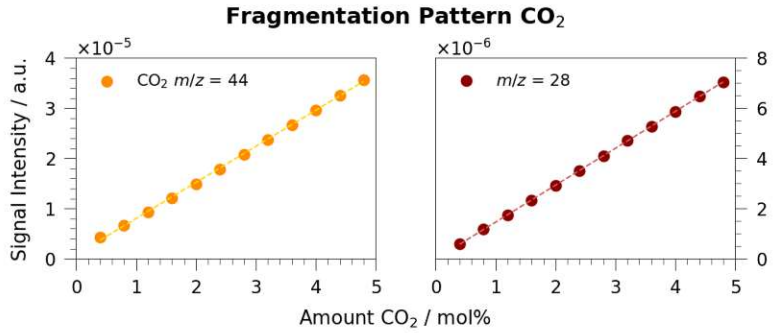

Figure 22 – Fragmentation Pattern of CO_2
Like methanol, CO_2 exhibits a specific fragmentation pattern correlating to ***a)*** *the proportion of CO_2 in the gas phase.* ***b)*** *Illustration of the corresponding CO fragment (m/z =28) at different amounts of CO_2.*

For the correction of the respective signals during the measurement the following correlation was formulated:

$$I_{44} = I_{44,\,CO_2} + I_{44,MeOH} \qquad \text{(Eq. 13)}$$

$$I_{28} = I_{28,CO} + I_{28,CO_2} + I_{28,MeOH} \qquad \text{(Eq. 14)}$$

I_{44} ..... *recorded signal of m/z ratio 44 (CO_2) / a.u.*
$I_{44,CO2}$ ..... *signal caused by CO_2 in reaction atmosphere / a.u.*
$I_{44,MeOH}$ ..... *signal caused by fragments of methanol / a.u.*

I_{28} ..... *recorded signal of m/z ratio 28 (CO) / a.u.*
$I_{28,CO}$ ..... *signal caused by CO in reaction atmosphere / a.u.*
$I_{28,CO2}$ ..... *signal caused by fragments of CO_2 / a.u.*
$I_{28,MeOH}$ ..... *signal caused by fragments of methanol / a.u.*

Using the obtained correlations described above the signals could be corrected with each measurement run respectively, according to the following equations:

$$I_{44,\,CO_2} = I_{44} - I_{44,MeOH} \quad \text{(Eq. 15)}$$

$$I_{28,CO} = I_{28} - I_{28,CO_2} - I_{28,MeOH} \quad \text{(Eq. 16)}$$

3.2.6. Amount of Reaction Gases

Using the information acquired in *Section 3.2.4.* and *Section 3.2.5.*, the composition of the gas phase throughout the reaction phase could be calculated. This was done in several steps. As no component exhibited fragments resulting in *m/z* ratios of 31 (MeOH), methanol was used as the starting point of the signal correction. Therefore, the first step consisted of the calculation of the proportion of methanol over the observation period. The second step was the determination of the fragmentation of methanol and the subsequent correction of the signals of the *m/z* ratios 44, 28 and 2. In the third step the fragmentation caused by CO_2 had to be calculated. For this the corrected signal of the component was used to determine its proportion in the gas phase. Utilising the fragmentation pattern obtained in the previous section we were able to determine the fragmentation of CO_2 correlated to its amount in the gas phase during the reaction period. The fourth and last step consisted of the correction of the remaining signals of CO and H_2 and the following calculation of their proportion in the reaction atmosphere.

```
## Correction of Raw Data using Fragmentation Pattern ---------------------------

def program correction

# import of calibration information necessary
# amount of methanol used as starting point of correction process
# information necessary for the evaluation of the formed fragments

        for data points of signal_MeOH:

                amount_MeOH = (y(signal_MeOH)-d(cal_MeOH)/k(cal_MeOH)

# correction according to obtained fragmentation patterns of MeOH
# use amount_MeOH for correction of signals via MeOH fragments
# calculate proportion of fragments
# subtract signal intensities of fragments from raw signals

        for data points of signal_CO2, signal_CO and signal_H2:

                correct data using fragmentation pattern of MeOH

# calculate amount of CO2

        for data points of signal_CO2:

                amount_CO2 = (y(signal_CO2)-d(cali_CO2)/k(cali_CO2)
```

```
# use amount_CO for correction of CO and H2 signals via CO2 fragments
# calculate proportion of fragments
# subtract signal intensities of fragments from raw signals

       for data points of signal_CO and signal_H2:

              correct data using fragmentation pattern of CO2

end program correction
```

Figure 23 – Implementation of Fragmentation Correction
To calculate the proportion of the reaction gases the fragmentation of the components methanol and CO_2 has to be taken into account. For this the signal of methanol is used as the starting point of the correction process. After the calculation of the proportion of methanol the amount of fragments formed can be calculated according to its specific fragmentation pattern. After correcting the signal intensities of H_2, CO and CO_2 the proportion of CO_2 within the reaction atmosphere can be determined. This information was again used to calculate the fragmentation of CO_2 according to its specific fragmentation pattern. The last steps consists of the correction of the signals of H_2 and CO and the determination of their proportion respectively.

3.2.7. Implementation of Individual Correction Factors

As illustrated in Figure 24a, the obtained data exhibited a shift in the Y-axis. This led to a significant loss of information in the evaluated data. This shift could be caused by incorrect determination of the baseline values and therefore an incorrect subtraction. As depicted in Figure 16 in *Section 3.2.2.*, the state of the system has a significant impact on the value of the individual baselines. Since the installation of the MeOH-H_2O disperser interferes with the system, the calculated baseline values may deviate from the actual ones.

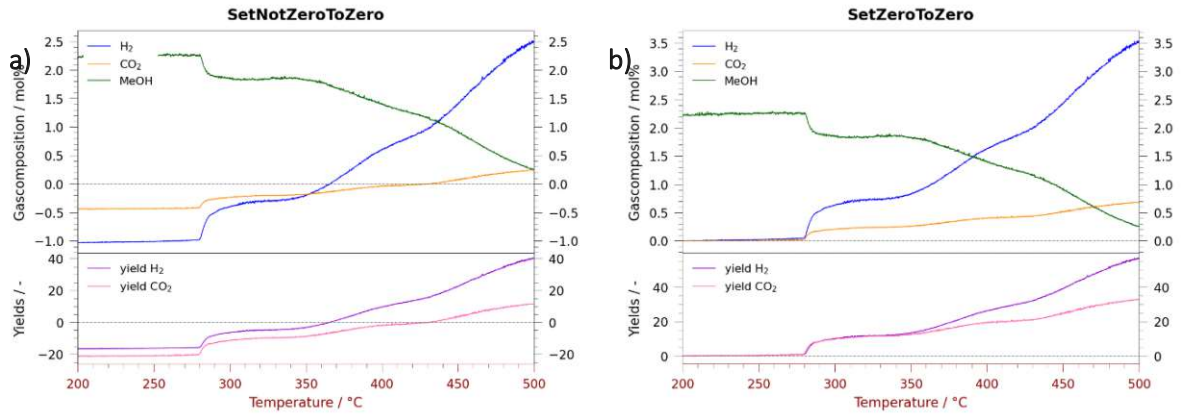

Figure 24 – Correction Factor
*Depiction of the data sets before **a)** and after **b)** the application of the individual correction factor of the respective components. Without any correction factor information is found below 0 mol%. Since the molar amount of the respective gases had to be zero at the beginning of the reaction phase, the deviation of the calculated value at this point was used to correct the data accordingly.*

For this reason we decided to apply individual correction factors after the evaluation process by introduction the starting point of the temperature ramp as an additional reference point. Since the gases H_2, CO_2 and CO were not present at the beginning of the reaction phase, their molar quantity at

the start of the observation period could be assumed to be zero. The difference between the received and the assumed quantity of the respective components was used to correct the respective data sets accordingly.

4. Results and Discussion

4.1. Synthesis

As in *Section 3.1.1.* described, after the synthesis of the materials NCF-CuX (X = 3 %, 5 %, 10 %) and PCF-CuX (X = 3 %, 5 %, 10 %), XRD measurements were carried out to determine the phase purity of the investigated catalysts. As depicted in Figure 25, no residues of the synthesis in the form of carbonates (CaCO3) could be found in any of the samples. However, we could demonstrate that a brownmillerite phase (shoulder at 33°) is formed under the prevailing synthesis conditions alongside the desired perovskite phase. This phase represents a complex oxide, similar to perovskite type oxides and takes a general form of $A_2B_2O_5$. [36]

It could be observed that the amount of Cu within the material affects the formation of this phase, as illustrated in Figure 25. Looking at NCF-based materials, for instance, lower amounts of Cu lead to reduced formation of the undesired phase indicated by a less pronounced shoulder in the reflex of the pristine material. For example, NCF-Cu10 displayed a much stronger expression of the shoulder associated with the brownmillerite phase than, NCF-Cu03. Interestingly, with PCF-based materials the catalysts with 5% Cu exhibit the biggest signal intensity of the reflection of the brownmillerite phase.

Additionally, it could be observed that the reflection positions were shifted to lower diffraction angles when the base material was doped with Cu. The incorporation of Cu atoms in the crystal lattice leads to an increase of the lattice parameters, whereby the corresponding reflections occur at lower angles (see Eq. 2).

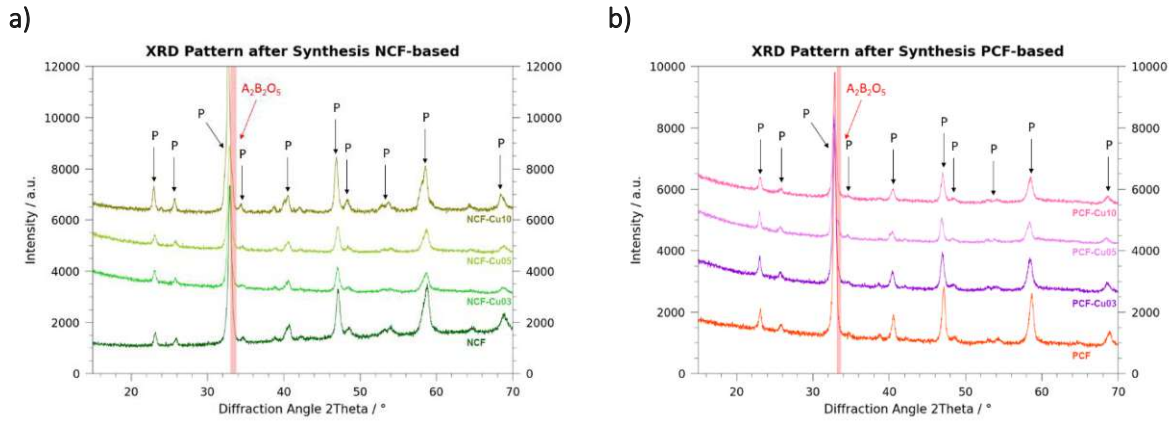

Figure 25 *– Diffractograms after Synthesis*
Illustration of the obtained diffractograms after the synthesis of ***a)*** *NCF based and* ***b)*** *PCF based catalysts. In addition to the desired formation of the pristine perovskite-based oxides (P), a brownmillerite phase* ($A_2B_2O_5$) *is formed during the synthesis under the prevailing conditions. This phase leads to a shoulder of the reflex at 33°.*

4.2. Validation of Evaluation Process

For the investigation of the suitability of quantitative investigation methods, the system used for the analysis has to be validated. This includes testing for repeatability as well as evaluating the error of evaluation, limit of detection and limit of quantification. [37]

4.2.1. Repeatability

To demonstrate the repeatability of analytical methods the relative standard deviation of these repetitions is used. According to Taverniers et al [37, p. 8], a limit value of 4 must not be exceeded for the concentration range used for this set-up. As depicted in Figure 26 below, this could be achieved for nearly all measurement points.

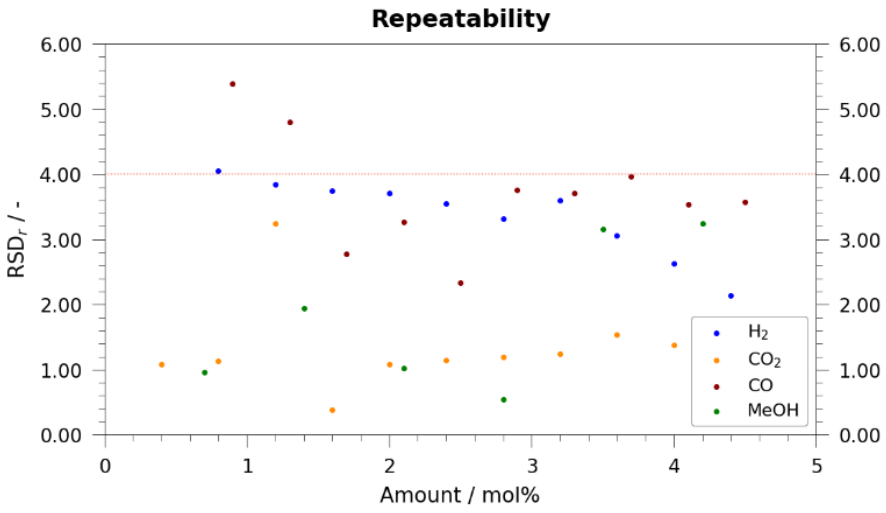

Figure 26 – Repeatability of Analysis Method
Almost every measurement displayed an acceptable RSD_r. The exception being only the lowest concentration measured for CO, were both RSD_r values exceeded the threshold of 4. This leads to the assumption that the repeatability of the measurement results is made more difficult at lower concentrations of CO.

As illustrated in Figure 26, all measurements of the gases H_2, CO_2 and MeOH display acceptable RSD_r values below 4, which is according to Taverniers et al [37, p. 8] the upper limit for acceptable measurement used for analytic methods. The same is also achieved when measuring CO in concentrations above 1.7 mol%. Below that concentration range the RSD_r values spikes to up to 5.38 for CO. These high values lead to the assumption that at lower concentrations the quantification of CO becomes more difficult in a single measurement.

4.2.2. Error of Evaluation

Furthermore, the bias of the investigation method was examined using the recovery yield of the respective gases. Nearly all of the recovery yields for the gases H_2, CO_2 and MeOH can be found within

an error range of ±10 %. For the lower concentrations of CO the recovery yield can be found in a 15 % range. The only exception here is H_2 at a concentration of 0.8 mol%. For evaluating these error values, gas atmospheres with a defined composition were measured repeatedly. The measured values were then compared with the true value of the individual data point to determine the error of evaluation. For this purpose the ratio of the measured to the true value was calculated respectively. The used gas composition and obtained measurement data can be found in the *Appendix*.

It could be determined that the smallest deviations from the true value could be achieved with methanol as the measuring gas. For methanol the recovery yields fluctuate between -7 % and +5 %. On the other hand, the highest deviations from the true values could be observed for H_2. At concentrations below 1.2mol% there are deviations of up to +28 %. In general, H_2 displays an overestimation of the measured values at lower concentrations, whereas above concentrations of 2 mol% there is an increasing underestimation. A similar behaviour could be observed with CO_2 but at a lesser degree. Furthermore, the bias of the measurements for CO_2 appears to reach a constant value above 2.4 mol%. CO displays a persistent underestimation of the true value ranging from -14 % to -6 %.

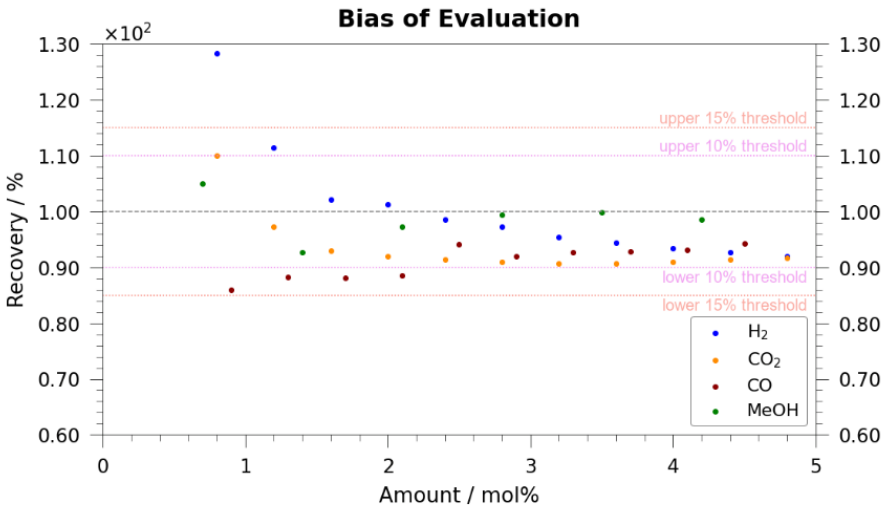

Figure 27 *– Validation of Method*
The reliability of the analysis method was examined using a precisely defined gas composition. Measured data points were compared with the true values using the respective ratio of measured versus true value.. It could be shown that there are varying deviations of the measured value compared to the true value, depending on the concentration and the investigated gas composition. The best accordance could be found for methanol over the whole concentration range, whereas for H_2 the highest deviation of the recovery yield was obtained.

4.2.3. Limits of Detection and Quantification

To determine the values for the limits of detection (LOD) and quantification (LOQ) the standard deviation of repeated blank measurements were used respectively, according to Equation 17.

$$LOD, LOQ = SD_{\text{blank}} \cdot k \quad \text{(Eq. 17)}$$

LOD ..... *Limit of Detection / %*
LOQ ..... *Limit of Quantification / mol-%*
k ..... *numerical factor / -*
SD_{blank} ..... *standard deviation of repeated blank measurements / mol-%*

The value of k is chosen according to the value of confidence necessary for LOD and LOQ. For the calculation of the LOD a value of 3 was used for k. This ensures that a measured value can be distinguished from reference measurements with a probability of 99%. For this, errors of type 1 and 2 are treated as the same. In the case of LOQ the k value was set to 10. With this a relative standard deviation of 10 % is achieved at the LOQ. [37, pp. 10–11]

The values obtained in this way for the LOD and LOQ of the respective measurement gases are summarized in Table 4.

Table 4 *– Limits of Detection and Quantification*

	H_2 / mol%	CO_2 / mol%	CO / mol%	MeOH / mol%
LOD	0.07	0.04	0.19	0.16
LOQ	0.22	0.13	0.63	0.54

4.3. Catalytic Measurements

For the investigation of the catalytic behaviour of the investigated materials the samples were tested according to the measurement procedure described in *Section 2.2.*. The obtained results are being summarised in the following chapter.

4.3.1. Reactor Data

All materials examined displayed catalytic activity towards MSR. By doping the base materials NCF and PCF with Cu, Co and Ni, an increase in catalytic activity compared to the undoped samples could be achieved. Furthermore, we were able to demonstrate that the choice of the dopant element significantly influences the properties of the material. Different doping materials exhibited differences in their on-set temperature and their selectivity towards the undesired formation of CO.

This is especially the case for Cu as dopant element. As illustrated in Figure 28, Cu dopant in varying degrees leads to a significant reduction in the on-set temperature. For example, the start of the formation of H_2 could be observed in a range of 272 °C to 285 °C, where NCF-Cu03 and NCF-Cu05 as

well as PCF-Cu03 and PCF-Cu05 displayed the lowest on-set temperature. Already at a temperature of 310 °C, conversion rates of up to 35 % could be observed, depending on the amount of Cu within the crystal structure. At the same time no significant amount of CO is formed under these conditions, meaning that high selectivity could be achieved at lower temperatures. In contrast, the undoped materials as well as materials doped with Ni and Co display neither significant formation of H_2 nor CO at 310 °C. The on-set temperatures for Ni and CO doped materials could found between 320 °C and 350 °C. For the undoped base structures the formation of H_2 only starts above 400 °C. With increasing temperature, an increase in the conversion rate could be determined for all materials examined. At 500 °C, for example, conversion rates of up to 100 % have been achieved, as depicted in the *Appendix*. However, at the same time the formation of CO increases in varying degrees.

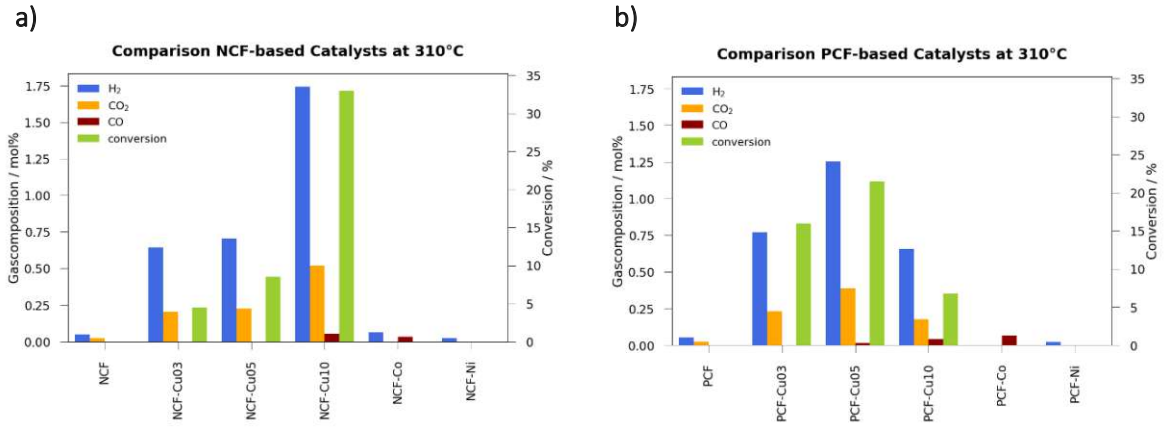

Figure 28 *– Catalytic Activity at 310 °C*
For lower temperatures the formation of H_2 could be observed for Cu-based materials. Both ***a)*** *NCF as well as* ***b)*** *PCF based materials displayed catalytic activity below 310 °C in various degrees. At these low temperatures no Formation of CO could be observed leading to a high selectivity of these materials towards MSR.*

As can be seen in Figure 29, the selectivity of the respective materials exhibit a high dependency on the reaction temperature. In general, it can be noted that in most cases, with higher temperature, there is an increased formation of CO and thus a reduction in selectivity. Exceptions are PCF-Co and PCF-Ni. These materials already display a low selectivity of around 80 % at low temperatures. However, this increases with rising temperatures and in the case of PCF-Co reaches 90 % at 500 °C. What also stands out in Figure 29 is the high selectivity for all materials which uses Cu as their B-site dopant. In a range from about 320 °C to 350 °C, a stable selectivity of around 100 % is achieved for both PCF and NCF-based materials with a Cu content of 3 % and 5 %. Above 350 °C this value starts to decrease, due to the increasing formation of CO, and drops to about 90 % at 500 °C.

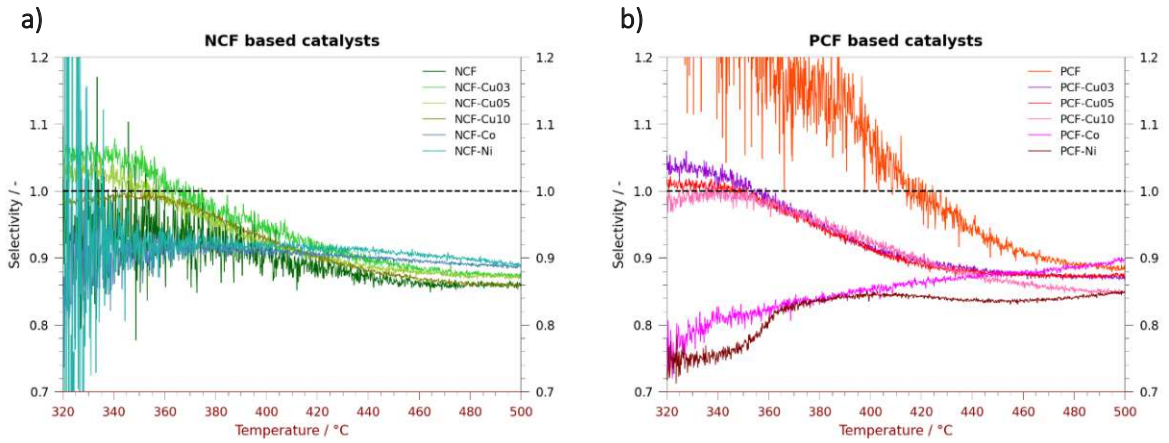

Figure 29 – Selectivity of Investigated Materials
Illustration of the temperature dependency of the selectivity of the respective materials. ***a)*** *Depiction of the changing selectivity of NCF-based materials with increasing temperature.* ***b)*** *Varying selectivity of PCF-based materials with increasing reaction temperature. Due to high noise at lower temperatures the selectivity can only be determined at higher temperatures, resulting in selectivity rates over 100 %.*

For materials doped with 10 % Cu interesting behaviour of the selectivity could be observed. Both NCF and PCF based catalyst displayed a relatively low selectivity of around 95 % at 280 °C – below that temperature no selectivity could be calculated due the high noise within the signals. This value increases with temperature and peaks at around 340 °C for PCF-Cu10 and 350 °C for NCF-Cu10 at 100 % selectivity. After that the signal development follows the same behaviour as the rest of the materials resulting in the lowest selectivity at 500 °C.

Another interesting aspect to look at is the carbon balance of the investigated materials over the observation period. Here, the amount of carbon is measured and monitored in the gas phase. This means that any deviation from 100 % indicates changes of the carbon content in the reaction atmosphere. For instance, a decrease could be tied to losses of carbon in the reactions atmosphere due to unwanted formation of carbonaceous solids on the surface of the catalyst, such as elemental carbon or some form of carbonate.

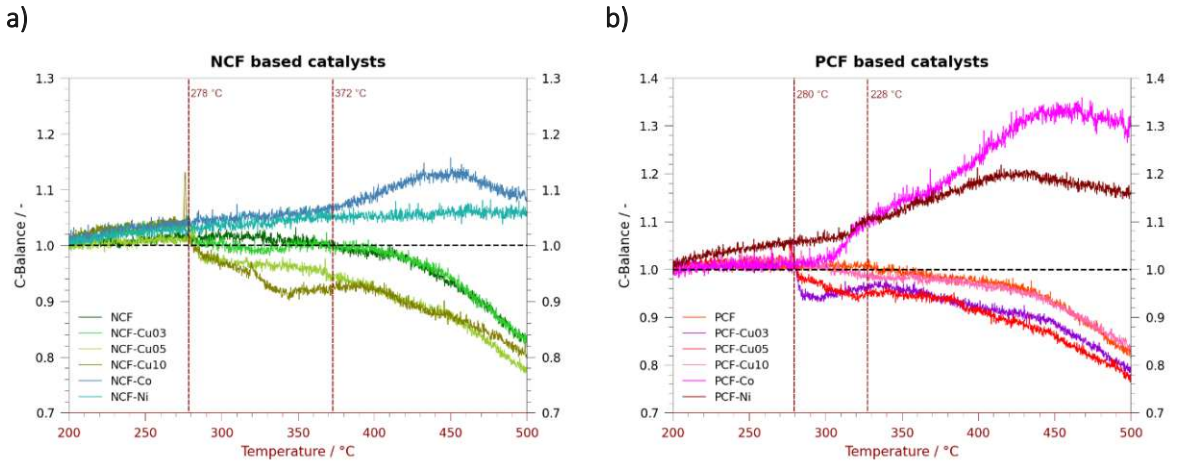

Figure 30 – *Carbon Balance*

*Illustration of the carbon balance over the observation period for **a)** NCF-based and **b)** PCF-based materials. Deviation of the C-balance at higher temperature for all materials investigated. The decrease at higher temperatures could be tied to possible formation of carbonates at perovskite surface. The unexpected increase is still part of ongoing investigation.*

The investigated catalysts differ in their respective behaviour of the carbon balance not only due to different doping elements, but also due to different doping content in the case of Cu, as illustrated in Figure 30. For example, NCF-Ni exhibits a constant carbon balance of 100 % over the observation period – the steady increase can be explained by a constant drift of the signal used for evaluating the carbon balance. The materials NCF, PCF as well as NCF-Cu03 and PCF-Cu03 all display similar behaviour with a constant carbon balance at lower temperatures and a steady decline at higher temperatures. In the case of NCF-based catalysts this deviation takes place at around 370 °C. For PCF-based materials this deviation already begins at lower temperatures of around 330 °C. Materials with a higher Cu content display an abrupt drop in the carbon balance at 280 °C. This can be observed for both NCF- as well as PCF-based catalysts with a Cu content of 5 % and 10 % respectively. The most interesting behaviour is displayed by the materials NCF-Co, PCF-Co and PCF-Ni. All of these materials exhibit an increase in their carbon balance which corresponds to a rising amount of carbon within in the gas atmosphere. A possible cause of this unusual behaviour could be impurities in the material. During synthesis using the Pecchini method, carbonaceous residues are removed by incineration. If this process is not complete, there is the possibility that the remaining residues will react with the reaction atmosphere as the temperature increases and form MS-active fragments. This then leads to a positive deviation of the carbon balance, as depicted in Figure 30.

All measurements and other measurement results including the specific activity of the individual catalyst can be found in more detail in the *Appendix*.

4.3.2. XRD Measurements

In addition to the catalytic reaction tests, a diffraction pattern of the catalyst was recorded after each test run and examined for possible phase changes that occurred during the observation period. For instance, it could be determined that all materials displayed the formation of a calcium carbonate phase, which correlates with the already obtained data in the sections above. Additionally, PCF as well as NCF exhibited the formation of an Fe_3O_4 phase which can be tied to exsolution of the B-site element iron in lack of any available dopant. The metallic nanoparticle which is formed during the reduction period is than oxidised over the reaction period and forms iron oxide on the surface of the bulk material.

For the catalysts doped with Cu a reflex at 43° indicates that metallic Cu was formed during the observation period. According to the varying intensities of this reflex a lower amount of Cu used for doping the B-site leads to a decreased amount of metallic Cu formed during the reduction period. This holds true for both PCF-based as well as NCF-based catalysts.

Metallic phases of the B-site doping could not be found for both Ni and Co doped materials. This could be explained by the signal intensity of the diffractograms being too low. Comparing the relative intensities of the respective diffractograms, it is noticeable that those of PCF-Ni, PCF-Co, NCF-Ni and NCF-Co are significantly lower compared to the rest of the data. Due to the finite sensitivity of the measuring device, it is possible that the reflections of the respective metallic phase cannot be distinguished from the noise. This is supported by the significantly increased catalytic activity of these materials compared to the undoped base materials. This increase in catalytic activity indicates that catalytically active metallic nanoparticles were indeed formed during the reduction phase but simply cannot be distinguished from noise in these diffractograms.

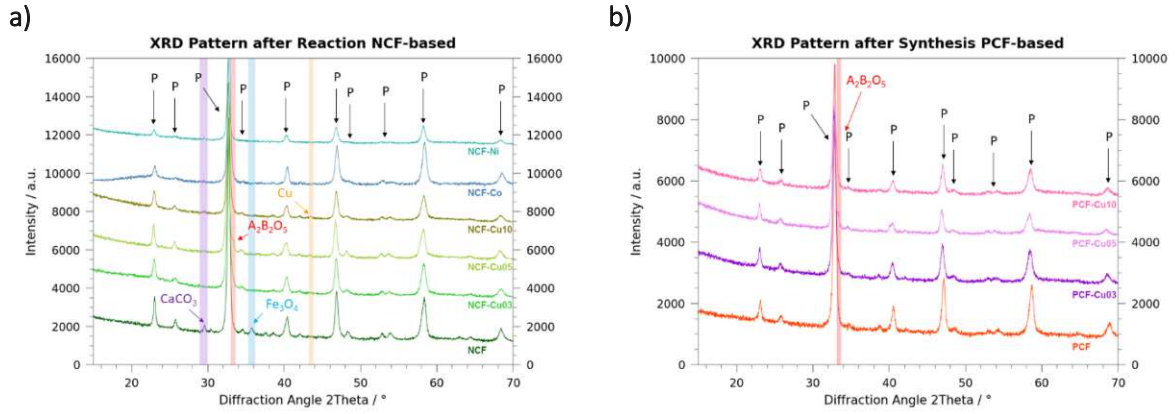

Figure 31 - Diffractograms after Reaction
*Illustration of the XRD measurement performed after the reaction period for **a)** NCF-based and **b)** PCF-based materials. All investigated materials exhibited the formation of calcium carbonate in varying degrees. For the undoped base structures the formation of Fe_3O_4 could be observed. Additionally, a metallic copper phase was detected for all Cu doped materials.*

4.4. *Operando* XRD

During the beamtime at DESY the following samples were investigated: NCF-Cu03, NCF-Cu10, PCF-Cu03, PCF-Cu10 as well as the undoped base structures NCF and PCF for comparison. Time resolved XRD measurements were performed to monitor possible phase changes during the observation period as described in *Section 2.2.3*. The results regarding PCF-Cu10 and NCF-Cu10 are illustrated in Figure 32 and 33. The remaining data is summarised in the *Appendix*.

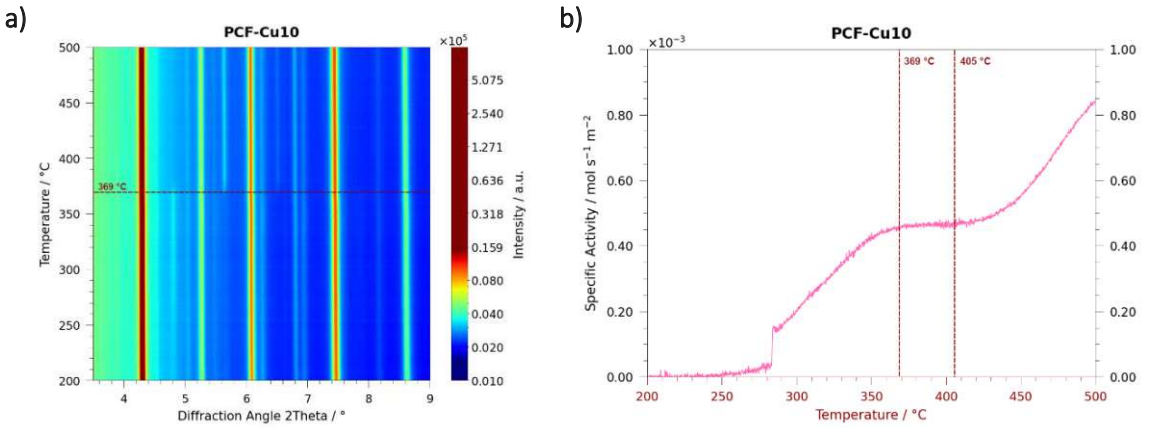

Figure 32 *– Operando XRD Measurement PCF-Cu10*
a) *Illustration of the obtained time resolved XRD measurement regarding possible phase changes in PCF-Cu10.* ***b)*** *Correlating the reaction measurements of PCF-Cu10 with data obtained via operando XRD. Deviations in the increase in specific activity could be tied to phase changes occurring at higher temperatures.*

As depicted in Figure 32a, successful exsolution during the reduction phase could be confirmed for PCF-Cu10. For example, at the start of the temperature ramp, reflexes were identified which can be assigned to the exsolution of Cu. The reflex found at 4.8° corresponds to Cu_2O, which means that the metallic nanoparticles of Cu is oxidised between the reduction and reaction phase. At around 369 °C formation of reflexes at diffraction angles of 5.7° and 6.5° can be observed. These reflexes correspond to the metallic Cu phase. Simultaneously the reflections for Cu_2O begins to decrease. This could be caused by a growing production of H_2 resulting in an increase in the reducing potential of the reaction atmosphere. With more H_2 within the gas mixture more Cu_2O can be reduced to form metallic nanoparticles again. This effect can also be noticed by looking at the behaviour of the specific activity over the observation period. As depicted in Figure 32b, the steady increase of the specific activity transitions into a steady phase at around 369 °C. In this phase the formed H_2 is used to reduce the Cu_2O phase and thus H_2 from the reaction mixture. Due to still increasing temperature this loss of H_2 is compensated by increasing catalytic activity of the material both caused by higher temperature as well as an increasing formation of catalytic active metallic Cu nanoparticles. At around 405 °C the specific activity begins to increase again. This could be to a turnover point in which H_2 is formed at a higher rate than it is consumed.

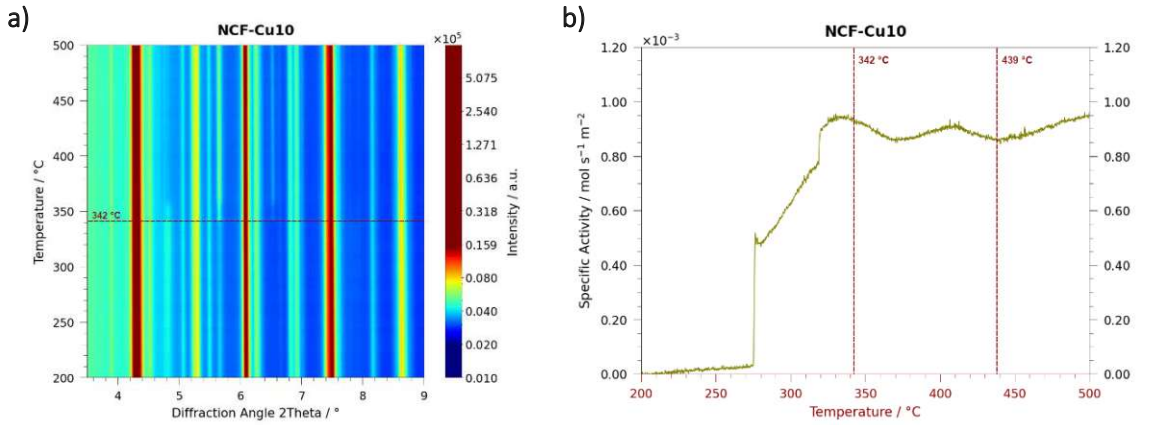

Figure 33 – Operando XRD Measurement NCF-Cu10
***a)** Illustration of the obtained time resolved XRD measurement regarding possible phase changes in NCF-Cu10. **b)** Correlating the reaction measurements of NCF-Cu10 with data obtained via operando XRD. Deviations in the increase in specific activity could be tied to phase changes occurring at higher temperatures.*

NCF-Cu10 behaves similarly to PCF-Cu10. A Cu_2O can also be found at the start of the reaction period, which is reduced to metallic Cu with rising temperatures and an increasing production of H_2. However, the reduction already starts at 342 °C. Same as with PCF-Cu10, this trend is also reflected in the behaviour of the specific activity of NCF-Cu10. However, no plateau is being formed at this temperature. Rather a fluctuating behaviour takes place. Only above a temperature of about 439°C does a stable increase in specific activity occur again.

4.4.1. SEM Analysis

In addition to operando XRD measurements, SEM images were taken of each material in order to examine its surface after a successful reaction phase. It could be confirmed that all investigated materials displayed the formation of nanoparticles. As illustrated in Figure 34, both 3 % Cu as well as 10 % Cu materials have been successfully exsolved. These exsolved nanoparticle are depicted in Figure 34. In general, it could be seen that the proportion of Cu influences the number of particles formed on the surface. Apparently higher dopant content stabilises the growth of nanoparticles which leads to an increase in exsolution under the same conditions. Furthermore, it could be observed that the formation of nanoparticles occurs in clusters for most of the materials, as illustrated in Figure 34. For NCF-Cu10 as well as for PCF-Cu03 and PCF-Cu10 nanoparticles were found in clusters on the surface of the material. For the base structures of PCF and NCF formation of nanoparticles were also observable but at a lesser degree. These formed particles were tied to the exsolution of Fe due to the lack of any dopant material.

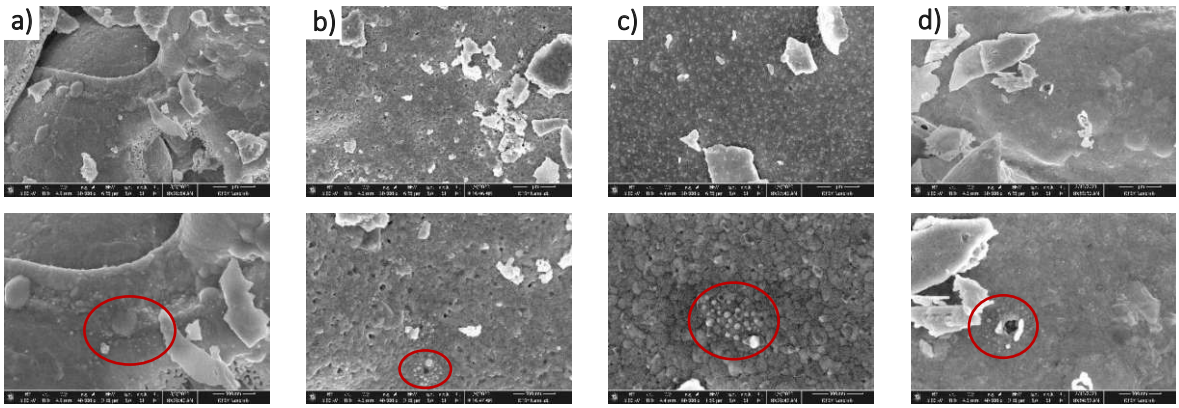

Figure 34 – SEM Images Operando XRD

*Depiction of SEM images of **a)** NCF-Cu03, **b)** NCF-Cu10, **c)** PCF-Cu03 as well as **d)** PCF-Cu10. Formation of nanoparticles on the surface of the materials could be confirmed. It could be observed that the formation of nanoparticles was more pronounced for those materials with 10 % Cu than those with 3 % Cu. Furthermore, nanoparticle could be found grouped in cluster formations.*

5. Conclusion

In this thesis, perovskite-type oxides were investigated regarding their potential for catalysing **M**ethanol **S**team **R**eforming (MSR). For this purpose, the materials were examined using catalytic test reactors as well as performing *operando* XRD measurements at DESY beamline P02.1. For the interpretation of the reactor measurements a calibration strategy for the quantitative evaluation of catalytic **m**ass **s**pectrometric (MS) data was successfully established using an external calibration approach. To simplify future implementation of this technique, a Python toolkit was developed for the automated evaluation of this data. During the calibration, a limitation of the quantification was observed for lower concentrations. For example, H_2 displayed a deviation from the true value of 28 % at concentrations below 1 mol%. In the case of CO, on the other hand, it could be demonstrated that the repeatability of measurement results is made considerably more difficult at concentrations below 1.2 mol%. However, it could be demonstrated that, in general the quantitative data obtained are repeatable, exhibiting RSD_r values below 4 and have a relatively low error rate of ± 10 % for H_2, CO_2 and methanol. CO displayed a slightly higher error rate of ± 15 %. Furthermore, the LOQ of the various reaction gases were determined ranging from 0.13 mol% for CO_2, 0.22 mol% for H_2, 0.54 mol% for methanol to 0.63 mol% for CO. In Future works, the improvement of this analysis method regarding lower concentration of the components should be emphasized.

With the implemented measuring procedure, it could be demonstrated that all investigated materials exhibited catalytic activity towards MSR. The materials that were doped with Cu in various concentration displayed the highest potential for the application as catalysts. For both the material classes of $Nd_{0.6}Ca_{0.4}Fe_{1-x}Cu_xO_3$ and $Pr_{0.6}Ca_{0.4}Fe_{1-x}Cu_xO_3$ (x = 0.03, 0.05, 0.1) a reduction in the on-set temperature, reaching below 290 °C could be observed. Those catalysts with a Cu doping of 3% and 5% displayed the lowest on-set temperature of about 270 °C. Furthermore, these materials exhibited relatively high conversion rates. In the case of $Nd_{0.6}Ca_{0.4}Fe_{0.9}Cu_{0.1}O_3$, conversion rates of 35 % were already observed at a temperature of 310 °C, followed by $Pr_{0.6}Ca_{0.4}Fe_{0.95}Cu_{0.05}O_3$ with a conversion rate of 23 %. In contrast, at these low temperatures, no conversion of the reaction educts could be observed with the undoped base structures and the materials which were doped with Co and Ni.

In addition to an increased catalytic activity by doping the B-sites with Cu, a greatly improved selectivity could be achieved. While no suppression of CO formation was observed for the undoped base structures $Nd_{0.6}Ca_{0.4}FeO_3$ and $Pr_{0.6}Ca_{0.4}FeO_3$, as well as those materials doped with Co and Ni, Cu-doped catalysts exhibited a selectivity of 100 % at certain temperature ranges. In the case of $Nd_{0.6}Ca_{0.4}Fe_{0.9}Cu_{0.1}O_3$ and $Pr_{0.6}Ca_{0.4}Fe_{0.9}Cu_{0.1}O_3$ this high selectivity only occurs in a very narrow temperature range around 350 °C

and 340 °C respectively. A larger temperature window of high selectivity could be observed for the catalysts doped with 3 % and 5 % Cu. For $Nd_{0.6}Ca_{0.4}Fe_{1-x}Cu_xO_3$ catalysts this window was around 60 °C, for materials with $Pr_{0.6}Ca_{0.4}Fe_{1-x}Cu_xO_3$ as their basis structure it was around 70 °C (see Table 5). It could thus be demonstrated that, in addition to the choice of the doping element, the amount of doping in the overall composition of the catalysts also plays a decisive role in terms of their catalytic activity and their selectivity towards MSR.

Table 5 *– Results Catalytic Measurements*
Comparison of the catalytic measurements monitored via mass spectrometry. The starting temperatures of methanol steam reforming could be reduced by doping the investigated materials with copper, cobalt and nickel. At the same time high selectivity could be achieved for copper doped materials at lower temperatures.

Catalysts	On-Set Temperature H_2-Formation / °C	On-Set Temperature CO-Formation / °C	CO free Temperature Range / °C
$Nd_{0.6}Ca_{0.4}FeO_3$	366	366	-
$Nd_{0.6}Ca_{0.4}Fe_{0.97}Cu_{0.03}O_3$	276	331	55
$Nd_{0.6}Ca_{0.4}Fe_{0.9}Cu_{0.05}O_3$	273	338	57
$Nc_{0.6}Ca_{0.4}Fe_{0.9}Cu_{0.1}O_3$	286	275	-*
$Nd_{0.6}Ca_{0.4}Fe_{0.9}Co_{0.1}O_3$	309	312	-
$Nd_{0.6}Ca_{0.4}Fe_{0.9}Ni_{0.1}O_3$	328	325	-
$Pr_{0.6}Ca_{0.4}FeO_3$	392	395	-
$Pr_{0.6}Ca_{0.4}Fe_{0.97}Cu_{0.03}O_3$	278	343	65
$Pr_{0.6}Ca_{0.4}Fe_{0.9}Cu_{0.05}O_3$	275	345	70
$Pr_{0.6}Ca_{0.4}Fe_{0.9}Cu_{0.1}O_3$	283	285	-*
$Pr_{0.6}Ca_{0.4}Fe_{0.9}Co_{0.1}O_3$	308	302	-
$Pr_{0.6}Ca_{0.4}Fe_{0.9}Ni_{0.1}O_3$	312	312	-

* *100 % seletivtiy could be achieved at a certain temperature (NCF-Cu10: 350 °C, PCF-Cu10: 340 °C)*

By analysing XRD data, recorded after the synthesis of the catalysts, it was possible to establish that under the given circumstances no phase-purity could be achieved. Rather, a brownmillerite phase (a complex oxide) is formed with the applied molar ratios of the elements used for the basis structures. But, in this thesis, neither a positive nor a negative influence of this phase on the catalytic activity of the respective materials could be quantified. Possible influences of the elementary composition of the basis

structures $Nd_{0.6}Ca_{0.4}FeO_3$ and $Pr_{0.6}Ca_{0.4}FeO_3$, as well as the effect of the brownmillerite phase formed during synthesis, on the catalytic effectiveness should be investigated in further research work.

Additional XRD measurements after the reaction as well as *operando* XRD measurements at the beamline P02.1 at DESY provided information about phase changes during the reaction conditions. For example, it could be demonstrated that $CaCO_3$ is deposited over the course of the reaction in all materials. This phenomenon leads to an inhibition of the catalytic activity, since the deposited $CaCO_3$ blocks otherwise catalytically active sites. This deposition of carbonates was also reflected in a decreasing carbon balance. Exceptions here were Co- and Ni-doped materials with an increasing carbon balance. The deviation from the expected behaviour is part of current research. One reason for this could be carbonaceous impurities, which are converted into gaseous components at higher temperatures and the environment becoming more reducing with an increased production of H_2. *Operando* XRD measurements revealed that formed nanoparticles of the Cu-doped materials are also subject to a phase change throughout the reaction. During the reduction using H_2, metallic Cu particles form on the surface. However, a CuO_2 phase could be identified at the beginning of the reaction phase. This could be explained by the fact that the metallic nanoparticles oxidise in the subsequent steps after reduction and form CuO_2. Only with an increased production of H_2 in the course of increased MSR activity does the reaction atmosphere become sufficiently reducing to convert CuO_2 back into metallic Cu. The reduction of the oxide during the reaction can be observed by the formation of reflections at 5.7° and 6.5°, which represent metallic Cu.

In summary, this work confirmed that Cu as a doping material creates the most suitable conditions for materials to be deployed as catalysts for MSR. By doping the B-site with Cu in different concentrations, both a high selectivity of 100% at low temperatures and an increased catalytic activity could be achieved. $Nd_{0.6}Ca_{0.4}Fe_{0.9}Cu_{0.1}O_3$ stands out with a conversion rate of 42% at 100% selectivity.

6. Summary

The advancing climate change and the threat it poses is causing an increase in the endeavour to decarbonise the energy sector e.g. using H_2 for the transport sector in the form of an energy carrier in e.g.: **P**roton **E**xchange **M**embrane Fuel Cells (PEMFC). **M**ethanol **S**team **R**eforming (MSR) provides a promising solution for the storage and on-demand production of H_2. However MSR requires high reaction temperatures and possible side reactions like the formation of carbon monoxide, which can lead to a significant performance loss of a PEMFC. Therefore, the use of suitable catalysts that reduce the on-set temperature and at the same time exhibit a high selectivity towards MSR in order to suppress the formation of unwanted side products are of crucial importance. A promising class of materials is the class of perovskite type oxides. These materials, with a general formula of ABO_3, possess the potential for high catalytic activity as well as high selectivity towards MSR. The composition of the catalyst can be specifically modified with suitable doping materials for the A- or B-site and can thus produce exsolved nanoparticles on its surface which fit the requirements necessary for MSR.

In this thesis, two types of catalysts were examined regarding their catalytic properties with respect to MSR: $Nd_{0.6}Ca_{0.4}Fe_{1-x}B_xO_3$ and $Pr_{0.6}Ca_{0.4}Fe_{1-x}B_xO_3$ (B = Cu: x = 0.03, 0.05, 0.1 / B = Ni, Co: x = 0.1). The goal was to achieve a reduced on-set temperature combined with high selectivity. The use of perovskite-type oxides as catalysts presents one decisive advantage: a process called Exsolution. Exposed to high temperatures and reducing environments these oxides exhibit the ability of exsolving highly active metallic nanoparticles on their surface. During this process, accumulation of B-site elements takes place. Doping the B-site with catalytic active elements such as Cu, Ni or Co can be used for tailoring the material to fit the necessary conditions of MSR. Caused by high reaction temperatures needed for MSR to take place, side reaction resulting in the unwanted production of CO also occur. As CO acts as catalyst poison, especially for conventional PEMCF catalytic anode materials, the formation of CO during MSR has to be supressed to prevent a loss of performance in the fuel cell.

For the investigation of the catalytic behaviour of the individual materials a **m**ass **s**pectrometer (MS) was utilised. For this purpose, a certain measurement procedure was implemented consisting of several steps. First, the material was oxidised to facilitate the same surface conditions. Second, reduction of the catalyst at elevated temperatures triggered exsolution of B-site elements. Third, the reaction atmosphere consisting of methanol and water in a molar ratio of 1:1 was equilibrated. Fourth, the respective catalyst was subjected to a temperature increase ranging from 200 °C to 500 °C to examine the catalytic activity of the material. Finally, reference points were measured to allow for a more precise quantification of the catalytic data obtained during the reaction. To be more precise, the measured

reference points were used to correct the temporal drift of the MS response. In addition to the development of the mentioned MS calibration scheme a Python script was developed for the automated evaluation of the MS data. Additionally, XRD measurements were performed after the reaction as well as *operando* XRD measurements at beamline P02.1 at DESY to examine possible changes during the temperature ramp.

It was found that all investigated materials exhibited catalytic activity towards MSR in various degrees, depending on the basis structure and element used for doping the B-site. Especially, Cu-doped materials excelled in their ability to reduce the necessary on-set temperature of the reaction as well as their high selectivity at lower temperatures. Although all materials displayed the formation of CO at elevated temperatures, stable selectivity rates of around 100 % could be achieved at temperatures of up to 350 °C for catalysts with a Cu content of 3 % and 5 %. For $Nd_{0.6}Ca_{0.4}Fe_{0.9}Cu_{0.1}O_3$ and $Pr_{0.6}Ca_{0.4}Fe_{0.9}Cu_{0.1}O_3$ a selectivity of 100 % could only be achieved at a small temperature range around 340 °C and 350 °C, respectively. Furthermore, XRD measurements revealed that all catalysts form an undesirable brownmillerite phase during synthesis. Furthermore, phase changes could be observed during the reaction. For example, it could be demonstrated that carbon is deposited in the form of carbonates. Moreover, the formation of a metallic Cu phase within the Cu-doped materials could be confirmed, which represents a successful exsolution of the B-site doping.

In summary, it could be demonstrated that perovskite-based oxides, in particular materials doped with Cu, represent a promising alternative to conventional catalysts. Due to their high resistance to sintering of the nanoparticles formed, these are particularly suitable for temperatures at which Cu particles in conventional materials already begin to sinter and thus lose part of their active surface.

7. Outlook

In this thesis it could be proven that all investigated catalysts exhibited catalytic activity towards MSR. Especially Materials doped with Cu in particular stood out regarding their high selectivity at lower temperatures. This property makes Cu-doped catalysts extremely attractive as possible competitors to conventional materials for catalysing MSR. Particularly interesting for further research would be their performance in comparison to commercial materials such as $Cu/ZnO/Al_2O_3$. In this regard, the investigation of other Cu-based materials, such as the class of cuprates, represents another promising approach to further decrease the necessary temperatures for MSR.

Additionally, measurements for testing different reduction temperatures of Cu doped materials should be performed. Different temperatures during the reduction period could be used to fine-tune the particle growth and size of the exsolved nanoparticles. The impact of these possible different sized nanoparticles on the catalytic activity towards MSR should be investigated by correlating MS data obtained during the reaction period with the achieved particle size at different reduction temperatures

Another important aspect is the in-depth analysis of the remaining DESY data. The behaviour of the materials during the reduction, heating and cooling phases is of particular interest here. In addition, measurements using Near Ambient Pressure XPS should be carried out to investigate the surface compositions of the most promising materials. With this, possible changes at the surface of the catalysts could be monitored helping the understanding of the behaviour during the reaction phases.

References

[1] 'Europäischer Grüner Deal', *EU-Kommission - European Commission*. https://ec.europa.eu/info/strategy/priorities-2019-2024/european-green-deal_de (accessed Sep. 27, 2021).

[2] 'Übereinkommen von Paris', *Klimapolitik - European Commission*, Nov. 23, 2016. https://ec.europa.eu/clima/policies/international/negotiations/paris_de (accessed Sep. 27, 2021).

[3] 'CO2-Emissionen von Autos: Zahlen und Fakten (Infografik) | Aktuelles | Europäisches Parlament', Mar. 22, 2019. https://www.europarl.europa.eu/news/de/headlines/society/20190313STO31218/co2-emissionen-von-autos-zahlen-und-fakten-infografik (accessed Sep. 23, 2021).

[4] C. E. Thomas, 'Fuel cell and battery electric vehicles compared', *Int. J. Hydrog. Energy*, vol. 34, no. 15, pp. 6005–6020, Aug. 2009, doi: 10.1016/j.ijhydene.2009.06.003.

[5] Y. Manoharan *et al.*, 'Hydrogen Fuel Cell Vehicles; Current Status and Future Prospect', *Appl. Sci.*, vol. 9, no. 11, Art. no. 11, Jan. 2019, doi: 10.3390/app9112296.

[6] M. Kayfeci, A. Keçebaş, and M. Bayat, 'Chapter 3 - Hydrogen production', *Sol. Hydrog. Prod. Process. Syst. Technol.*, pp. 45–83, Jan. 2019, doi: https://doi.org/10.1016/B978-0-12-814853-2.00003-5.

[7] R. Ning *et al.*, 'On-demand production of hydrogen by reacting porous silicon nanowires with water', *Nano Res.*, vol. 13, no. 5, pp. 1459–1464, May 2020, doi: 10.1007/s12274-020-2734-8.

[8] F. Xu and X. Liu, '"On–Off" Control for On-Demand Hydrogen Production from the Dehydrogenation of Formic Acid', *ACS Catal.*, vol. 11, no. 22, pp. 13913–13920, Nov. 2021, doi: 10.1021/acscatal.1c03923.

[9] D. Reynard, G. Bolik-Coulon, S. Maye, and H. H. Girault, 'Hydrogen production on demand by redox-mediated electrocatalysis: A kinetic study', *Chem. Eng. J.*, vol. 407, p. 126721, Mar. 2021, doi: 10.1016/j.cej.2020.126721.

[10] D. Ventura-Espinosa, S. Sabater, A. Carretero-Cerdán, M. Baya, and J. A. Mata, 'High Production of Hydrogen on Demand from Silanes Catalyzed by Iridium Complexes as a Versatile Hydrogen Storage System', *ACS Catal.*, vol. 8, no. 3, pp. 2558–2566, Mar. 2018, doi: 10.1021/acscatal.7b04479.

[11] D. R. Palo, R. A. Dagle, and J. D. Holladay, 'Methanol Steam Reforming for Hydrogen Production', *Chem. Rev.*, vol. 107, no. 10, pp. 3992–4021, Oct. 2007, doi: 10.1021/cr050198b.

[12] T. A. Rocha, F. Ibanhi, F. Colmati, J. J. Linares, V. A. Paganin, and E. R. Gonzalez, 'Nb as an influential element for increasing the CO tolerance of PEMFC catalysts', *J. Appl. Electrochem.*, vol. 43, no. 8, pp. 817–827, Aug. 2013, doi: 10.1007/s10800-013-0572-z.

[13] L. Lindenthal *et al.*, 'Ca-doped rare earth perovskite materials for tailored exsolution of metal nanoparticles', *Acta Crystallogr. Sect. B Struct. Sci. Cryst. Eng. Mater.*, vol. 76, no. 6, Art. no. 6, Dec. 2020, doi: 10.1107/S2052520620013475.

[14] T. Berger, 'Methanol Steam Reforming Using Perovskite Catalysts'. Dec. 21, 2021.

[15] S. Xing, C. Zhao, S. Ban, Y. Liu, and H. Wang, 'Thermodynamic performance analysis of the influence of multi-factor coupling on the methanol steam reforming reaction', *Int. J. Hydrog. Energy*, vol. 45, no. 11, pp. 7015–7024, Feb. 2020, doi: 10.1016/j.ijhydene.2019.12.192.

[16] S. Sá, H. Silva, L. Brandão, J. M. Sousa, and A. Mendes, 'Catalysts for methanol steam reforming—A review', *Appl. Catal. B Environ.*, vol. 99, no. 1, pp. 43–57, Aug. 2010, doi: 10.1016/j.apcatb.2010.06.015.

[17] M. Behrens and M. Armbrüster, 'Methanol Steam Reforming', in *Catalysis for Alternative Energy Generation*, L. Guczi and A. Erdôhelyi, Eds., New York, NY: Springer, 2012, pp. 175–235. doi: 10.1007/978-1-4614-0344-9_5.

[18] B. Frank, F. C. Jentoft, H. Soerijanto, J. Kröhnert, R. Schlögl, and R. Schomäcker, 'Steam reforming of methanol over copper-containing catalysts: Influence of support material on microkinetics', *J. Catal.*, vol. 246, no. 1, pp. 177–192, Feb. 2007, doi: 10.1016/j.jcat.2006.11.031.

[19] N. Han *et al.*, 'Superior three-dimensional perovskite catalyst for catalytic oxidation', *EcoMat*, vol. 2, no. 3, p. e12044, 2020, doi: 10.1002/eom2.12044.

[20] J. Popovic *et al.*, 'High Temperature Water Gas Shift Reactivity of Novel Perovskite Catalysts', *Catalysts*, vol. 10, no. 5, Art. no. 5, May 2020, doi: 10.3390/catal10050582.

[21] Z. Bian, Z. Wang, B. Jiang, P. Hongmanorom, W. Zhong, and S. Kawi, 'A review on perovskite catalysts for reforming of methane to hydrogen production', *Renew. Sustain. Energy Rev.*, vol. 134, p. 110291, Dec. 2020, doi: 10.1016/j.rser.2020.110291.

[22] M. A. Peña and J. L. G. Fierro, 'Chemical Structures and Performance of Perovskite Oxides', *Chem. Rev.*, vol. 101, no. 7, pp. 1981–2018, Jul. 2001, doi: 10.1021/cr980129f.

[23] Q. A. Islam, S. Paydar, N. Akbar, B. Zhu, and Y. Wu, 'Nanoparticle exsolution in perovskite oxide and its sustainable electrochemical energy systems', *J. Power Sources*, vol. 492, p. 229626, Apr. 2021, doi: 10.1016/j.jpowsour.2021.229626.

[24] D. Neagu *et al.*, 'Nano-socketed nickel particles with enhanced coking resistance grown in situ by redox exsolution', *Nat. Commun.*, vol. 6, no. 1, p. 8120, Nov. 2015, doi: 10.1038/ncomms9120.

[25] O. Kwon *et al.*, 'Exsolution trends and co-segregation aspects of self-grown catalyst nanoparticles in perovskites', *Nat. Commun.*, vol. 8, no. 1, p. 15967, Jun. 2017, doi: 10.1038/ncomms15967.

[26] L. Spieß, G. Teichert, R. Schwarzer, H. Behnken, and C. Genzel, *Moderne Röntgenbeugung: Röntgendiffraktometrie für Materialwissenschaftler, Physiker und Chemiker*, 2., Überarb. und erw. Aufl. in Studium. Wiesbaden: Vieweg + Teubner, 2009.

[27] P. Willmott, 'An introduction to synchrotron radiation: techniques and applications', *Choice Rev. Online*, vol. 49, no. 11, pp. 49-6341-49–6341, Jul. 2012, doi: 10.5860/CHOICE.49-6341.

[28] E. Ellersdorfer, 'Methanoldampfreformierung auf Palladium basierten Katalysatoren'. Apr. 2019.

[29] '6 Mass spectrometers and residual gas analysis'. https://www.pfeiffer-vacuum.com/en/know-how/mass-spectrometers-and-residual-gas-analysis/introduction-operating-principle/ (accessed Sep. 14, 2021).

[30] '6.3 Quadrupole mass spectrometers (QMS)'. https://www.pfeiffer-vacuum.com/en/know-how/mass-spectrometers-and-residual-gas-analysis/quadrupole-mass-spectrometers-qms/quadrupole-mass-filter/ (accessed Sep. 14, 2021).

[31] M. P. Pechini, 'Method of preparing lead and alkaline earth titanates and niobates and coating method using the same to form a capacitor', US3330697A, Jul. 11, 1967 Accessed: Sep. 13, 2022. [Online]. Available: https://patents.google.com/patent/US3330697A/en

[32] J. A. B. da Silva, F. G. B. Moreira, V. M. L. dos Santos, and R. L. Longo, 'On the hydrogen bond networks in the water–methanol mixtures: topology, percolation and small-world', *Phys. Chem. Chem. Phys.*, vol. 13, no. 14, pp. 6452–6461, Apr. 2011, doi: 10.1039/C0CP01802C.

[33] A. Hartono and I. Kim, 'Calculation of Vapor-Liquid Equilibria for Methanol-Water Mixture using Cubic-Plus-Association Equation of State'. 2004.

[34] K. Yang, X. Fang, R. W. Gross, and X. Han, 'A practical approach for determination of mass spectral baselines', *J. Am. Soc. Mass Spectrom.*, vol. 22, no. 11, pp. 2090–2099, Nov. 2011, doi: 10.1007/s13361-011-0229-2.

[35] V. K. Dobruskin, 'Effect of Chemical Composition on Enthalpy of Evaporation and Equilibrium Vapor Pressure', *ArXiv10043400 Cond-Mat Physicsphysics*, Apr. 2010, Accessed: Aug. 23, 2021. [Online]. Available: http://arxiv.org/abs/1004.3400

[36] J. Young and J. M. Rondinelli, 'Crystal structure and electronic properties of bulk and thin film brownmillerite oxides', *Phys. Rev. B*, vol. 92, no. 17, p. 174111, Nov. 2015, doi: 10.1103/PhysRevB.92.174111.

[37] I. Taverniers, M. De Loose, and E. Van Bockstaele, 'Trends in quality in the analytical laboratory. II. Analytical method validation and quality assurance', *TrAC Trends Anal. Chem.*, vol. 23, no. 8, pp. 535–552, Sep. 2004, doi: 10.1016/j.trac.2004.04.001.

List of Figures

List of Tables

List of Formulas

Page	Formular	Number
9	$t = \frac{r_A + r_O}{\sqrt{2 \times (r_B + r_O)}}$	(Eq. 1)
12	$2 \cdot d_{hkl} \cdot \sin(q) = n \cdot \lambda$	(Eq. 2)
13	$B = \frac{\Phi}{\Delta\Omega \cdot \frac{\Delta\lambda}{\lambda}}$	(Eq. 3)
22	$Y_{H_2} = \frac{n_{H_2}}{3 \cdot n_{MeOH}} \cdot 100\%$	(Eq. 4)
22	$Y_{CO_2} = \frac{n_{CO_2}}{n_{MeOH}} \cdot 100$	(Eq. 5)
23	$X_{MeOH} = 1 - \frac{n_{MeOH}}{n_{MeOH,0}} \cdot 100$	(Eq. 6)
23	$\dot{V}(X_{MeOH}) = \dot{V}(0) + \varepsilon \cdot \dot{V}(0) \cdot \frac{n_{MeOH}}{n_{MeOH} + n_{CO_2}} \cdot x_{MeOH} \cdot Z$	(Eq. 7)
24	$specific\ activity = \frac{n_{CO_2} \cdot \dot{V}(X_{MeOH})}{S \cdot V_N}$	(Eq. 8)
24	$selectivity = \frac{\sum n_{desired}}{\sum n} \cdot 100$	(Eq. 9)
31	$y_i = f \cdot k \cdot x_i + d$	(Eq. 10)
31	$f = \frac{y_i - d}{k \cdot x_i}$	(Eq. 11)
32	$\Delta(\Delta H) = -R \cdot T \cdot \ln(\frac{p}{p_s})$	(Eq. 12)

List of Formulas

Page	Formular	Number
34	$I_{44} = I_{44,\,CO_2} + I_{44,MeOH}$	(Eq. 13)
34	$I_{28} = I_{28,CO} + I_{28,CO_2} + I_{28,MeOH}$	(Eq. 14)
35	$I_{44,\,CO_2} = I_{44} - I_{44,MeOH}$	(Eq. 15)
35	$I_{28,CO} = I_{28} - I_{28,CO_2} - I_{28,MeOH}$	(Eq. 16)
41	$LOD, LOQ = SD_{blank} \cdot k$	(Eq. 17)

List of Abbreviations

Abbreviation	Definition	Unit
FC	Fuel Cell	-
PEMFC	Proton Exchange Membrane Fuel Cell	-
XRD	X-Ray Diffraction	-
SEM	Scanning Electron Microscopy	-
MS	Mass Spectrometer	-
MSR	Methanol Steam Reforming	-
DM	Decomposition of Methanol	-
WGS	Water-Gas-Shift	-
t	Goldschmidt tolerance factor	-
r_a	Radius of A-site element	Å
r_B	Radius of B-site element	Å
r_O	Radius of oxygen	Å
MFC	Mass Flow Controller	-
PID	Proportional Integral Derivative	-
SEM	Secondary Electron Multiplier	-
GC	Gas Chromatography	-
MeOH	Methanol	-
d_{hkl}	Lattice Plane Space	Å
λ	Wavelength	nm
B	Brilliance	Sch
Φ	Photon Flux	$s^{-1}\ m^{-2}$
Y_x	Yield	%
n_x	Molar Amount	mol%
RSD	Relative Standard Deviation	%
RSD_r	RSD of Repeated Measurements	%

Appendix

I. Records Measurements

Enclosed are all collected reactor measurements, including the data used for the evaluation:

– Cloud - Reactor Measurements –

II. Python Script for Evaluation

For the purposes of this diploma thesis a Python script was written for the automated execution of the evaluation of the MS data. The script is attached in the following link:

– Cloud - Evaluation Script –

III. Supplemental Material

Table 6 *– Additional Information of Investigated Catalysts*
List of reduction temperature, masses as well as active surfaces of the investigated catalysts.

Catalysts	Relative Surface / $m^2\ g^{-1}$	Mass m / g	Absolute Surface / m^2	Reduction Temperature T / °C
NCF	5.520	0.0235	0.1297	700
NCF-Co	4.760	0.0258	0.123	575
NCF-Ni	-	0.0244	-	625
NCF-Cu10	4.530	0.2350	1.065	500
NCF-Cu05	2.709	0.0231	0.063	500
NCF-Cu03	2.603	0.0230	0.059	500
PCF	2.300	0.0233	0.054	700
PCF-Co	3.160	0.0241	0.076	575
PCF-Ni	-	0.0228	-	625
PCF-Cu10	4.520	0.0226	0.102	500
PCF-Cu05	3.597	0.0237	0.085	500
PCF-Cu03	3.290	0.0223	0.073	500

Table 7 –Settings for the Measurement via Mass Spectrometer
List of the measured m/z ratios necessary for the quantitative evaluation. Additionally, the dwell times of the respective component, flow rates of the respective reaction gases argon, hydrogen, and oxygen, and the used working pressure. The oxidative pre-treatment was performed using an oxygen flow of 10 ml min^{-1} with an additional flow of argon of 10 ml min^{-1}. During reaction an argon flow of 20 ml min^{-1} was passed through the methanol-water mixture.

Reaction Gas	Flow Rate / ml min^{-1}	*m/z* Ratio / -	Dwell Time t / ms	Working Pressure p / mbar
Hydrogen	20	2	8	$1.0 – 1.1 \times 10^{-6}$
Water	-	18	16	
Carbon monoxide	-	28	256	
Methanol	-	29	1024	
Methanol	-	31	1024	
Oxygen	20	32	512	
Argon	20	40	64	
Carbon dioxide	-	44	8	

Table 8 – Precursor Compounds for Sample Preparation
List of the utilised precursor compounds for the synthesis of the individual perovskite-type oxides. For the synthesis a modified Pechini method was performed.

Compound	NCF	PCF	Cu-doped	Co-doped	Ni-doped
Nd_2O_3	✓	-			
$CaCO_3$	✓	✓	✓	✓	✓
Compound	**NCF**	**PCF**	**Cu-doped**	**Co-doped**	**Ni-doped**
Fe	✓	✓	✓	✓	✓
$Pr_2(CO_3)_3 \times 8H_2O$	-	✓			
Cu	-	-	✓	-	-
$Co(NO_3)_2 \times 6H_2O$	-	-	-	✓	-
$Ni(NO_3)_2 \times 6H_2O$	-	-	-	-	✓

Table 9 – Parameters Baseline Correction

List of parameters for the determination of the baseline value for each signal. The values in the table below were obtained empirically and can be adapted when necessary. The parameters "window size" and "threshold" were used for determining the start of the baseline. The mean value of the individual baseline of the respective m/z ratios could be calculated using the parameters "upper limit" and "lower limit" which are the permitted percentage deviation of the value of the starting point.

Signal	Window Size	Threshold	Upper Limit	Lower Limit
H_2	170	15×10^{-7}	1.4	0.5
CO_2	-	-	1.4	0.6
CO	-	-	1.4	0.7
MeOH	-	-	1.8	0.4

Table 10 – Calibration of Methanol

Set temperatures for the calibration of methanol as well as a calculation scheme of the respective proportion of methanol in the reaction atmosphere.

Temperature / °C	p_{MeOH} / bar	$p_{(MeOH + H2O)}$ / bar	p_{total} / bar	Amount MeOH / mol%
0.0	7.1×10^{-3}	1.4×10^{-2}		0.7
12.8	1.4×10^{-2}	2.8×10^{-2}		1.4
20.2	2.1×10^{-2}	4.3×10^{-2}	1.013	2.1
25.6	2.8×10^{-2}	5.7×10^{-2}		2.8
29.7	3.5×10^{-2}	7.1×10^{-2}		3.5

Table 11 – External Calibration

List of calibration points for the components H_2, CO_2 and CO. A total flow of 50 ml $min^{-1}$was set. For each point the flow of the individual components were diluted with argon in varying degrees.

Component	Amount / mol%											
H_2	-	0.8	1.2	1.6	2.0	2.4	2.8	3.2	3.6	4.0	4.4	4.8
CO_2	0.4	0.8	1.2	1.6	2.0	2.4	2.8	3.2	3.6	4.0	4.4	4.8
CO	-	0.9	1.3	1.7	2.1	2.5	2.9	3.3	3.7	4.1	4.5	-

Table 12 – Validation Measurements for H_2

List of settings for a defined gas composition for the validation of the analysis method. Using the set and measured values the deviation of the respective measurement was calculated.

Set Amount / mol%	Measured Amount / mol%	Error / %	RSD_r / -	LOD / mol%	LOQ / mol%
0.8	1.03	128	4.06		
1.2	1.34	111	3.84		
1.6	1.63	102	3.74		
2.0	2.03	101	3.70		
2.4	2.37	99	3.54		
2.8	2.72	97	3.31	0.07	0.22
3.2	3.05	95	3.59		
3.6	3.40	94	3.06		
4.0	3.73	93	2.63		
4.0	4.08	93	2.14		
4.8	4.42	92	1.76		

Table 13 – Validation Measurements for CO_2

Set Amount / mol%	Measured Amount / mol%	Error / %	RSD_r / -	LOD / mol%	LOQ / mol%
0.4	0.53	133	1.08		
0.8	0.88	110	1.14		
1.2	1.17	97	3.25		
1.6	1.49	93	0.39		
2.0	1.84	92	1.09		
2.4	2.19	91	1.15	0.04	0.13
2.8	2.55	91	1.20		
3.2	2.90	91	1.24		
3.6	3.26	91	1.54		
4.0	3.64	91	1.38		
4.4	4.02	91	1.37		

Table 14 – Validation Measurements for CO

Set Amount / mol%	Measured Amount / mol%	Error / %	RSD_r / -	LOD / mol%	LOQ / mol%
0.9	0.77	86	5.38		
1.3	1.15	88	4.80		
1.7	1.50	88	2.78		
2.1	1.86	89	3.27		
2.5	2.35	94	2.34	0.19	0.63
2.9	2.67	92	3.76		
3.3	3.06	93	3.71		
3.7	3.44	93	3.96		
4.1	3.82	93	3.54		
4.5	4.24	94	3.57		

Table 15 – Validation Measurements for methanol

Set Amount / mol%	Measured Amount / mol%	Error / %	RSD_r / -	LOD / mol%	LOQ / mol%
0.7	0.74	105	0.96		
1.4	1.30	93	1.94		
2.1	2.04	97	1.02	0.16	0.54
2.8	2.78	99	0.55		
3.5	3.49	100	3.15		
4.2	4.14	98	3.25		

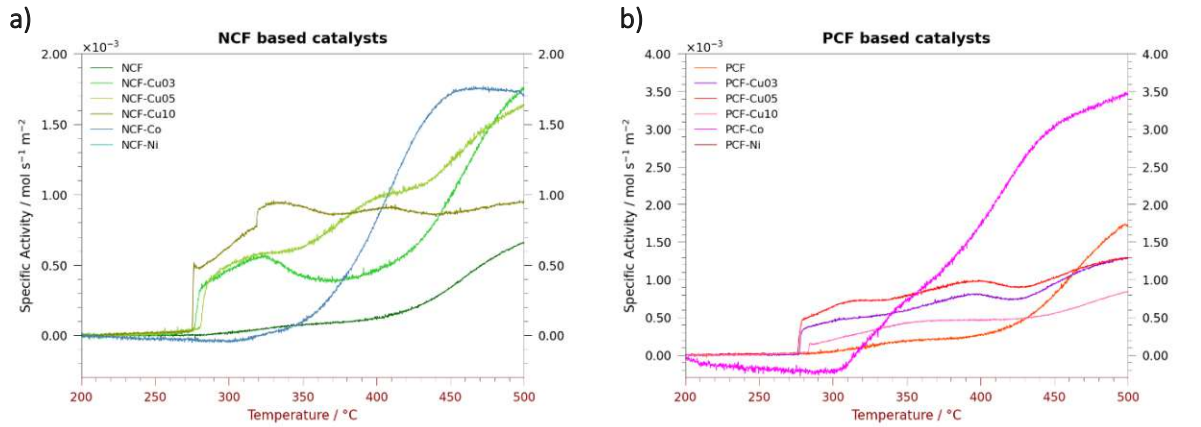

Figure 35 – *Specific Activity*

*Rates of specific activity for **a)** NCF-based und **b)** PCF-based materials. The specific activity is normalized using the surfaces of the respective catalysts. Illustration of the impact of the doping elements for the B-site of the basis material. The highest specific activity at lower temperatures could be achieved with materials doped with Cu.*

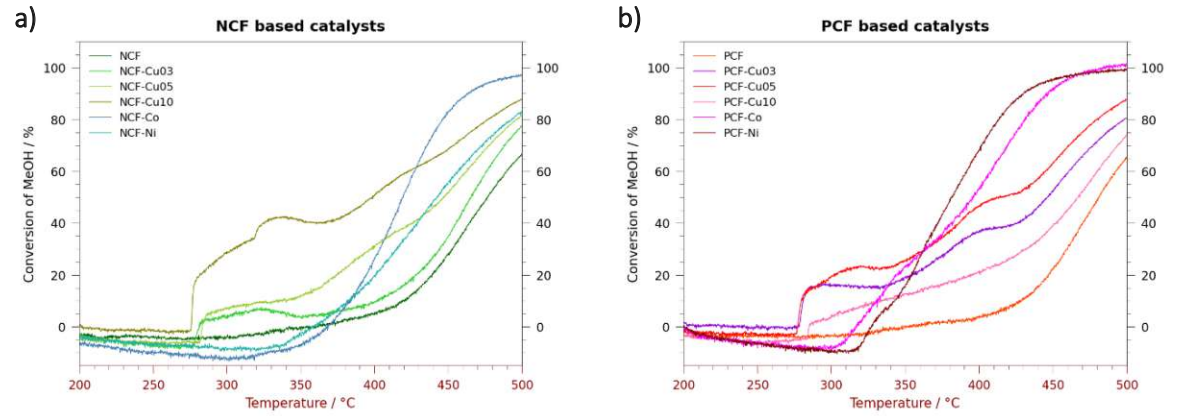

Figure 36 – *Conversion Rate*

*Depiction of the conversion rate of methanol for **a)** NCF-based and **b)** PCF-based materials. Generally, at higher temperatures higher conversion rates could be achieved for all materials investigated. The on-set temperature an the rate of conversion various greatly depending on the element used for doping the B-site.*

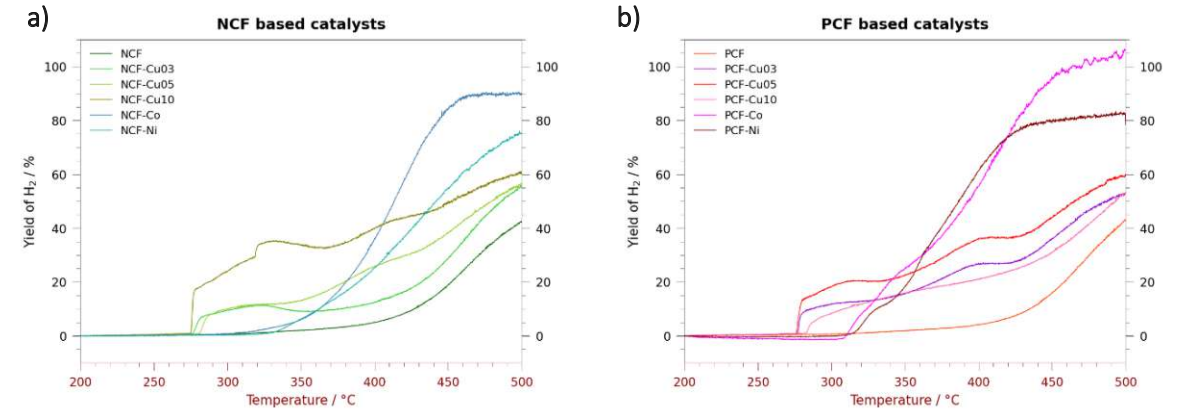

Figure 37 – *Yield of H_2*

*Illustration of the varying yields of hydrogen for **a)** NCF-base und **b)** PCF-based materials. The lowest on-set temperature was achieved with Cu as dopant element. The highest yield at 500 °C was achieved with NCF-Co and with PCF-Co, which both displayed reaching a thermodynamic limit above 450 °C indicated by the declining slope of the signal development.*

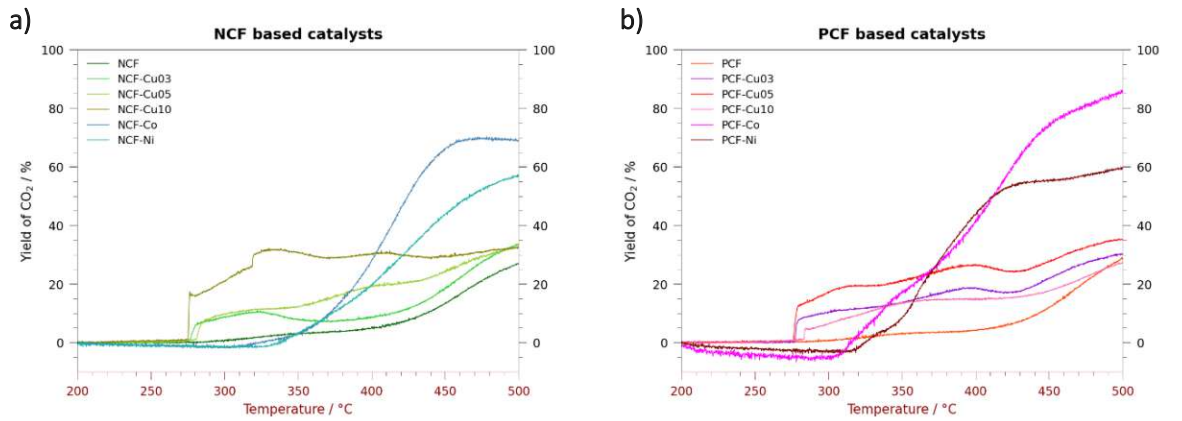

Figure 38 – Yield of CO_2

*Illustration of the varying yields of CO_2 for **a)** NCF-base und **b)** PCF-based materials. The lowest on-set temperature was achieved with Cu as dopant element. The highest yield at 500 °C was achieved with NCF-Co and with PCF-Co, which both displayed reaching a thermodynamic limit above 450 °C indicated by the declining slope of the signal development.*

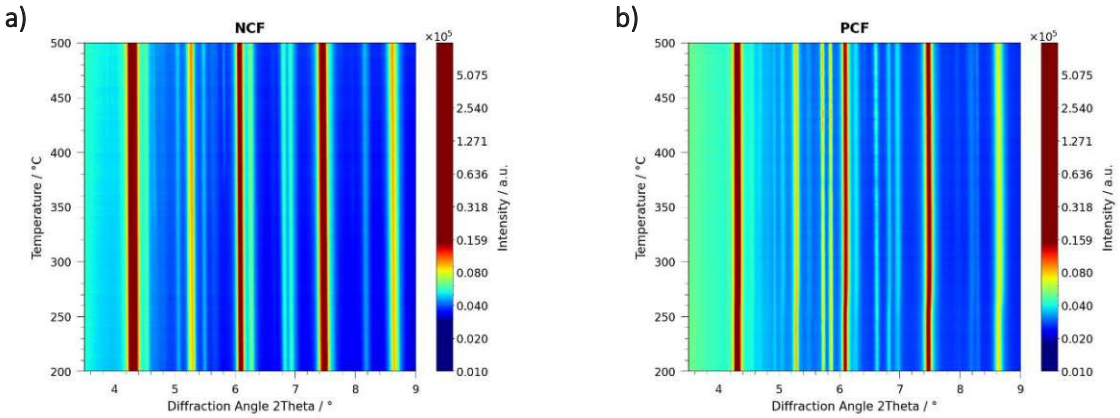

Figure 39 – Operando XRD Measurements for NCF and PCF

*Obtained data at DESY beamline P02.1 during operando XRD Measurement under MSR conditions. Illustration of phase changes for **a)** NCF and **b)** PCF during a temperature ramp of 200 °C to 500 °C.*

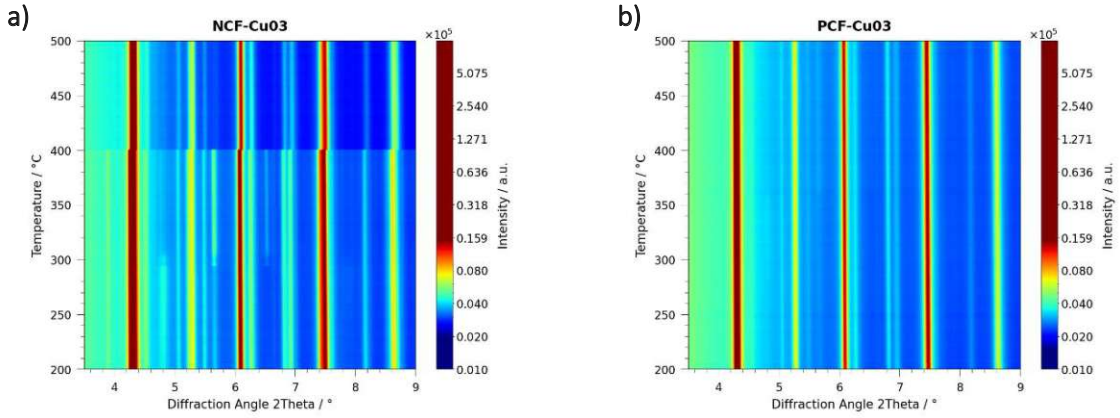

Figure 40 – Operando XRD Measurements for NCF-Cu03 and PCF-Cu03

*Obtained data at DESY beamline P02.1 during operando XRD Measurement under MSR conditions. Illustration of phase changes for **a)** NCF-Cu03 and **b)** PCF-Cu03 during a temperature ramp of 200 °C to 500 °C. For NCF-Cu03, the shift of the individual reflexes combined with a loss of signal intensity at 400 °C indicates a movement of the sample during the experiment.*